Upper bound on angular momentum transport in Taylor-Couette flow

Zijing Ding*
Department of Applied Mathematics and Theoretical Physics, University of Cambridge, Cambridge CB3 0WA, England, United Kingdom

Elena Marensi
School of Mathematics and Statistics, University of Sheffield, Sheffield S3 7RH, England, United Kingdom

(Received 6 July 2019; published 24 December 2019)

We investigate the upper bound on angular momentum transport in Taylor-Couette flow theoretically and numerically by a one-dimensional background field method. The flow is bounded between a rotating inner cylinder of radius R_i and a fixed outer cylinder of radius R_o. A variational problem is formulated and solved by a pseudo-time-stepping method up to a Taylor number $\mathrm{Ta} = 10^9$. The angular momentum transport, characterized by a Nusselt number Nu, is bounded by $\mathrm{Nu} \leqslant c\mathrm{Ta}^{1/2}$, where the prefactor c depends on the radius ratio $\eta = R_i/R_o$. Three typical radius ratios are investigatedi.e., $\eta = 0.5,\ 0.714,$ and 0.909, and the corresponding prefactors $c = 0.0049,\ 0.0075,$ and 0.0086 are found to improve (lower) the rigorous upper bounds by Doering and Constantin [C. Doering and P. Constantin, Phys. Rev. Lett. **69**, 1648 (1992)] and Constantin [P. Constantin, SIAM Rev. **36**, 73 (1994)] by at least one order of magnitude. Furthermore, we show, via an inductive bifurcation analysis, that considering a three-dimensional background velocity field is unable to lower the bound.

DOI: 10.1103/PhysRevE.100.063109

I. INTRODUCTION

Liquid flow between two independently rotating concentric cylinders, known as the Taylor-Couette flow, has attracted much attention due to its vast relevance and numerous applications in geophysical and astrophysical systems, e.g., planetary atmospheres and stellar interiors. A problem of crucial interest, both from a practical and from a fundamental point of view, is to determine the global flux of angular momentum (or torque) between the cylinders and its scaling dependence on the parameters of the system (e.g., the rotation frequencies). To understand the complicated interplay between the boundary layers and the bulk in the turbulent regime, we aim to derive a rigorous estimate of such scaling directly from the governing equations, thus avoiding expensive calculations at large parameters values.

The first measurement of the angular momentum in Taylor-Couette flow dates back to the pioneering experiments of Wendt [1] in the 1930s. A huge body of experimental studies on the global torque scaling in the turbulent regime was then performed in the past 30 years [2–7]. As suggested by Eckhardt *et al.* [8], the angular momentum transfer can be characterized by a Nusselt number Nu, defined as the ratio of the turbulent angular velocity transport to the purely molecular (laminar) transport. The Nusselt number is measured against the Taylor number:

$$\mathrm{Ta} = \frac{(1+\eta)^4}{64\eta^2} d^2 (R_i + R_o)^2 (\Omega_i - \Omega_o)^2 / \nu^2. \tag{1}$$

Here R_i and R_o are the inner and outer radii, $d = R_o - R_i$ is the gap width, $\eta = R_i/R_o$ is the radius ratio, Ω_i and Ω_o are the angular velocities of the inner and outer cylinders, and ν is the kinematic viscosity of the fluid. Experimental data showed that $\mathrm{Nu} \sim \mathrm{Ta}^{1/3}$ when the boundary layer is laminar, while $\mathrm{Nu} \sim \mathrm{Ta}^{1/2}$ with a logarithmic correction (due to the logarithmic velocity profile in the boundary layer) when the boundary layer is turbulent [9–11]. In their experimental study, van den Berg *et al.* [12] showed that, when the logarithmic velocity profile in the boundary layers is destroyed by wall roughness, the scaling of $\mathrm{Nu} \sim \mathrm{Ta}^{1/2}$ emerges because the angular momentum transport is determined by the bulk. This was also confirmed very recently by Zhu *et al.* [13] using direct numerical simulations (DNS).

DNS of turbulent Taylor-Couette flow between two smooth cylinders for three typical radius ratios $\eta = 0.5,\ 0.714,$ and 0.909 suggest that $\mathrm{Nu} \sim \mathrm{Ta}^{0.38}$ for $\eta = 0.714$ and 0.909 and $\mathrm{Nu} \sim \mathrm{Ta}^{1/3}$ for $\eta = 0.5$, up to $\mathrm{Ta} = 10^{11}$ [14–19]. It thus appears from these studies that the scaling depends on the geometry. Furthermore, direct numerical simulations have some shortcomings, such as the dependence on the initial conditions. It would be prohibitively expensive to find the optimal flow field that can maximize the angular momentum transport using DNS.

An alternative way to extract the scaling in turbulent flows without direct numerical simulations is to derive upper bounds on the angular momentum transport from a variational problem. This approach was established by Malkus [20] and Howard [21] for Rayleigh-Bénard convection and extended to plane Couette flow by Busse [22] (referred to as the MHB formulation). To solve the MHB variational problem, Nickerson [23] considered a single boundary layer and derived an upper bound of angular momentum transfer in Taylor-Couette flow, later improved by Busse [24] by including three nested boundary layers. However, Busse's result is not a strict upper bound because higher order terms, which tend to lower the upper bound, are neglected. In the

*z.ding@damtp.cam.ac.uk

1990s, an alternative approach, called the "background flow" method, was introduced by Doering & Constantin [25–27] to produce rigorous upper bounds of energy dissipation and heat transport. This method decomposes the physical field into a steady background field and an arbitrary fluctuation field and has the advantage that even a trial background field can yield an upper bound. Kerswell [28,29] proved that the "background" approach yields a minimization problem, which is complementary to the maximization problem in the MHB formulation.

Most early works [25–27,30] considered a one-dimensional piecewise-linear trial background field, which only produced a suboptimal upper bound on the heat and angular momentum transfer in Rayleigh-Bénard convection and Taylor-Couette flow, respectively. It was later shown by Plasting and Kerswell [31] that the optimal background field, which yields the lowest upper bound, can be obtained by solving the full set of Euler-Lagrange equations for the minimization problem numerically. The challenge is then to find the optimal "background field" satisfying the so-called "spectral constraint" [25–27,30]. This problem was first cracked by Plasting and Kerswell [31], in their study of plane-Couette flow, using a Newton-Raphson technique. Newton's method requires a bifurcation analysis of the "spectral constraint." Recently, Wen *et al.* [32,33] suggested an alternative, easy-to-implement, approach, which utilizes a pseudo-time-stepping method to solve the Euler-Lagrange equations without the need of a bifurcation analysis.

This paper applies the background method to investigate the upper bound problem of angular momentum transport in Taylor-Couette flow. The resulting variational problem is solved using the newly developed pseudo-time-stepping method [32,33]. First, we consider a one-dimensional background field, which, as we shall show later, leads to a variational problem with the surface-averaged momentum equation and the energy balance imposed as constraints. Our results improve (lower) the rigorous upper bound by Doering and Constantin [25] and Constantin [30] and the numerical studies by Nickerson [23] and Busse [24] by at least one order of magnitude. Second, we examine whether a three-dimensional background field can lower the bound by imposing the time averaged momentum equations as a constraint. The plan of the paper is as follows. Section II describes the mathematical formulation and Sec. III applies the one-dimensional background approach, which yields the variational problem. In Sec. IV, the Euler-Lagrange equations are derived from the variational formulation. Section V illustrates our numerical technique for solving the Euler-Lagrange equations. Results and discussions of the one-dimensional background approach are presented in Sec. VI. Section VII considers a three-dimensional background velocity field and an inductive bifurcation analysis is carried out. Conclusions are drawn in Sec. VIII.

II. MATHEMATICAL FORMULATION

A Newtonian incompressible fluid of kinematic viscosity ν fills the gap between two coaxial, independently rotating, cylinders. We consider a cylindrical coordinate system with the z axis as the common cylinder axis, and r and θ as the radial and azimuthal coordinates, respectively. The dimensionless governing equations (continuity and Navier-Stokes) obtained by choosing the gap width $d = R_o - R_i$ as length scale, and d^2/ν and ν/d as time and velocity scales, respectively, read

$$\nabla \cdot \boldsymbol{u} = 0, \tag{2}$$

$$\frac{\partial \boldsymbol{u}}{\partial t} + \boldsymbol{u} \cdot \nabla \boldsymbol{u} + \nabla p - \nabla^2 \boldsymbol{u} = 0, \tag{3}$$

where the velocity $\boldsymbol{u} = u\boldsymbol{e}_r + v\boldsymbol{e}_\theta + w\boldsymbol{e}_z$. Boundary conditions at $r = r_i, r_o$ ($r_i = R_i/d$, $r_o = R_o/d$) are

$$u = w = 0, \quad v|_{r=r_i} = \mathrm{Re}_i \equiv \frac{\Omega_i R_i d}{\nu},$$
$$v|_{r=r_o} = \mathrm{Re}_o \equiv \frac{\Omega_o R_o d}{\nu}. \tag{4}$$

The laminar flow has an azimuthal component only, $v = V_{\mathrm{lam}}(r)$, independent of θ and z, which is given by

$$V_{\mathrm{lam}} = Ar + \frac{B}{r}, \quad A = \frac{\omega_o - \eta^2 \omega_i}{1 - \eta^2}, \quad B = \frac{\eta^2(\omega_i - \omega_o)}{(1 - \eta^2)(1 - \eta)^2} \tag{5}$$

where $\omega_i = \mathrm{Re}_i/r_i$ and $\omega_o = \mathrm{Re}_o/r_o$ are the dimensionless angular velocities. We define a volume-temporal average $\langle \bullet \rangle$ and a surface-temporal average $\overline{\bullet}$:

$$\langle \bullet \rangle = \lim_{T\to\infty} \frac{1}{T} \frac{1}{\pi\Gamma\left(r_o^2 - r_i^2\right)} \int_{r_i}^{r_0} \bullet r dr d\theta dz dt\,, \tag{6}$$

$$\overline{\bullet} = \lim_{T\to\infty} \frac{1}{T} \frac{1}{2\pi\Gamma} \int_0^T \int_0^\Gamma \int_0^{2\pi} \bullet d\theta dz dt, \tag{7}$$

where Γ is the axial length of the domain. Following Eckhardt *et al.* [8], by taking the surface-temporal average of the azimuthal momentum equation we obtain

$$\frac{1}{r^2} \frac{d\overline{r^2 uv}}{dr} = \frac{d^2\overline{v}}{dr^2} + \frac{1}{r}\frac{d\overline{v}}{dr} - \frac{\overline{v}}{r^2}. \tag{8}$$

Introducing an angular velocity $\omega = v/r$, Eq. (8) is restated as

$$\frac{dJ^\omega}{dr} = \frac{d}{dr}\left[r^3\left(\overline{u\omega} - \frac{d\overline{\omega}}{dr}\right)\right] = 0, \tag{9}$$

where the conserved quantity $J^\omega \equiv r^3(\overline{u\omega} - d\overline{\omega}/dr)$ is the transverse current of angular velocity [8]. At the laminar state, $J^\omega_{\mathrm{lam}} \equiv 2\eta(\mathrm{Re}_i r_o - \mathrm{Re}_o r_i)/(1 - \eta^2)$, and the ratio $\mathrm{Nu} = J^\omega/J^\omega_{\mathrm{lam}}$ is defined, in analogy with the Rayleigh-Bénard problem, as the Nusselt number.

From the kinetic energy balance it follows that the viscous dissipation is connected to the angular momentum transport via

$$\varepsilon = \langle |\nabla \boldsymbol{u}|^2 \rangle - 2\frac{\mathrm{Re}_o^2 - \mathrm{Re}_i^2}{r_o^2 - r_i^2} = \frac{2(\omega_i - \omega_o)}{r_o^2 - r_i^2}$$
$$J^\omega_{\mathrm{lam}}\mathrm{Nu} = \mathrm{Pr}^{-2}\mathrm{TaNu}, \tag{10}$$

where $\mathrm{Pr} = \frac{(1+\eta)^4}{16\eta^2}$ is a geometrical "quasi-Prandtl" number (the analog of the Prandtl number in Rayleigh-Bénard convection) and the Taylor number was defined in Eq. (1). Once the dependence of the energy dissipation ε on the Taylor number is known, we can derive the relationship between Nu and Ta.

Our aim is to reveal this relationship using the "background" method [25–27].

III. ONE-DIMENSIONAL BACKGROUND METHOD

We decompose the velocity field as

$$\boldsymbol{u} = \boldsymbol{u}_b + \boldsymbol{u}' \tag{11}$$

where $\boldsymbol{u}_b = V(r)\boldsymbol{e}_\theta$ is a (steady) one-dimensional background field which carries the boundary conditions on v at $r = r_i, r_o$ (i.e., $V|_{r_i} = \mathrm{Re}_i$ and $V|_{r_o} = \mathrm{Re}_o$), and $\boldsymbol{u}'(\boldsymbol{x}, t)$ is an arbitrary fluctuation field which satisfies homogeneous boundary conditions. Now, we write the momentum equation (3) as

$$\begin{aligned}\boldsymbol{\mathcal{N}} := {} & \frac{\partial \boldsymbol{u}'}{\partial t} + \boldsymbol{u}_b \cdot \boldsymbol{\nabla}\boldsymbol{u}_b + \boldsymbol{u}_b \cdot \boldsymbol{\nabla}\boldsymbol{u}' + \boldsymbol{u}' \cdot \boldsymbol{\nabla}\boldsymbol{u}_b \\ & + \boldsymbol{u}' \cdot \boldsymbol{\nabla}\boldsymbol{u}' + \boldsymbol{\nabla} p - \nabla^2 \boldsymbol{u}' - \nabla^2 \boldsymbol{u}_b = 0. \end{aligned} \tag{12}$$

Using the decomposition in Eq. (11), the energy dissipation rate is expressed as

$$\begin{aligned}\varepsilon = {} & \langle |\boldsymbol{\nabla}\boldsymbol{u}'|^2 \rangle + \left\langle \left(\frac{dV}{dr}\right)^2 + \frac{V^2}{r^2} + 2\frac{dV}{dr}\frac{\partial v'}{\partial r} + \frac{2Vv'}{r^2} \right\rangle \\ & - 2\frac{\mathrm{Re}_o^2 - \mathrm{Re}_i^2}{r_o^2 - r_i^2}. \end{aligned} \tag{13}$$

The laminar viscous dissipation rate,

$$\varepsilon_{\mathrm{lam}} = \frac{4}{(1+\eta)^2}(\mathrm{Re}_i - \eta \mathrm{Re}_o)^2 \propto \mathrm{Ta}, \tag{14}$$

gives the lower bound on energy dissipation rate.

To find the maximal viscous dissipation rate, we construct the following Lagrangian:

$$\mathscr{L} := \varepsilon - \langle a\boldsymbol{u}' \cdot \boldsymbol{\mathcal{N}} \rangle = \varepsilon - \langle a(\boldsymbol{u} - \boldsymbol{u}_b) \cdot \boldsymbol{\mathcal{N}} \rangle. \tag{15}$$

The balance parameter a ensures the energy balance condition is satisfied in the system, namely, $\langle \boldsymbol{u} \cdot \boldsymbol{\mathcal{N}} \rangle = 0$, while the one-dimensional Lagrange multiplier $a\boldsymbol{u}_b$ imposes the surface-averaged azimuthal momentum equation. Integration by parts of Eq. (15) gives

$$\begin{aligned}\mathscr{L} = {} & \left\langle \left(\frac{dV}{dr}\right)^2 + \frac{V^2}{r^2} \right\rangle - 2\frac{\mathrm{Re}_o^2 - \mathrm{Re}_i^2}{r_o^2 - r_i^2} \\ & - \left\langle (a-1)|\boldsymbol{\nabla}\boldsymbol{u}'|^2 + au'v'\left(\frac{dV}{dr} - \frac{V}{r}\right) \right\rangle \\ & + \left\langle (a-2)\left(\frac{d^2V}{dr^2} + \frac{1}{r}\frac{dV}{dr} - \frac{V}{r^2}\right)v' \right\rangle. \end{aligned} \tag{16}$$

The presence of the linear term $(a-2)(\frac{d^2V}{dr^2} + \frac{1}{r}\frac{dV}{dr} - \frac{V}{r^2})v'$ in Eq. (16) means that the optimization over the fluctuation fields v' will give rise to a nonzero contribution to be added to $\langle (\frac{dV}{dr})^2 + \frac{V^2}{r^2} \rangle$. Following Plasting and Kerswell [31], we avoid this complication by defining a shifted fluctuation field:

$$\hat{u} = u', \quad \hat{v} = v' - \frac{2-a}{2(a-1)}\left(V - Ar - \frac{B}{r}\right), \quad \hat{w} = w'. \tag{17}$$

This is possible if $\hat{\boldsymbol{u}}$ is assumed to satisfy homogeneous boundary conditions and allows the linear term to be absorbed into perfect squares. As a result, a mean azimuthal velocity profile can be defined as

$$v_m = V + \frac{2-a}{2(a-1)}\left(V - Ar - \frac{B}{r}\right), \tag{18}$$

and Eq. (16) is restated as

$$\begin{aligned}\mathscr{L} = {} & \frac{a^2}{4(a-1)}\left\langle \left[\frac{d(V - V_{\mathrm{lam}})}{dr}\right]^2 + \frac{(V - V_{\mathrm{lam}})^2}{r^2} \right\rangle \\ & + \varepsilon_{\mathrm{lam}} - \mathscr{H}, \end{aligned} \tag{19}$$

where

$$\mathscr{H} = \left\langle (a-1)|\boldsymbol{\nabla}\hat{\boldsymbol{u}}|^2 + a\hat{u}\hat{v}\left(\frac{dV}{dr} - \frac{V}{r}\right) \right\rangle$$

is a quadratic form which is positive semidefinite provided $a > 1$ and V is well chosen. Furthermore, we introduce a new parameter $b = a/(a-1)$ $(b > 1)$ and the Lagrangian is modified as

$$\begin{aligned}\mathscr{L} = {} & \frac{b^2}{4(b-1)}\left\langle \left[\frac{d(V - V_{\mathrm{lam}})}{dr}\right]^2 + \frac{(V - V_{\mathrm{lam}})^2}{r^2} \right\rangle \\ & + \varepsilon_{\mathrm{lam}} - \frac{1}{b-1}\mathscr{H}, \end{aligned} \tag{20}$$

where the quadratic term is modified as

$$\mathscr{H} = \left\langle |\boldsymbol{\nabla}\hat{\boldsymbol{u}}|^2 + b\hat{u}\hat{v}\left(\frac{dV}{dr} - \frac{V}{r}\right) \right\rangle. \tag{21}$$

Therefore, the upper bound on the energy dissipation rate is

$$\begin{aligned}\varepsilon \leqslant \varepsilon_{\max} := {} & \frac{b^2}{2(b-1)\left(r_o^2 - r_i^2\right)} \\ & \times \int_{r_i}^{r_o} r\left\{ \left[\frac{d(V - V_{\mathrm{lam}})}{dr}\right]^2 + \frac{(V - V_{\mathrm{lam}})^2}{r^2} \right\} dr + \varepsilon_{\mathrm{lam}}, \end{aligned} \tag{22}$$

provided the quadratic term $\mathscr{H}$ is positive semidefinite, i.e., $\mathscr{H} \geqslant 0$, for all fluctuations $\hat{\boldsymbol{u}}$. The so-called spectral constraint $\mathscr{H} \geqslant 0$ is equivalent to the following nonpositive eigenvalue problem:

$$\lambda\hat{\boldsymbol{u}} = 2\nabla^2\hat{\boldsymbol{u}} - b\left(\frac{dV}{dr} - \frac{V}{r}\right)\begin{pmatrix}\hat{v}\\ \hat{u}\\ 0\end{pmatrix} - \boldsymbol{\nabla} p, \tag{23}$$

$$\boldsymbol{\nabla} \cdot \hat{\boldsymbol{u}} = 0, \tag{24}$$

where p is a Lagrange multiplier to impose the continuity equation. For a given background field V, the spectral constraint is satisfied provided that $\lambda \leqslant 0$.

IV. EULER-LAGRANGE EQUATIONS

Our aim is to minimize $\varepsilon_{\max}$ to produce the best upper bound on the viscous dissipation rate under the spectral constraint and the conservation of mass. The following Lagrange functional is thus identified:

$$\mathscr{L} = \varepsilon_{\max} - \mathscr{H} + \langle p\boldsymbol{\nabla} \cdot \hat{\boldsymbol{u}} \rangle. \tag{25}$$

Here, the velocity field $\hat{\boldsymbol{u}}$ is rescaled as $\hat{\boldsymbol{u}}/\sqrt{b-1} \to \hat{\boldsymbol{u}}$ for convenience. First variations of $\mathscr{L}$ yield the Euler-Lagrange equations

$$\delta\mathscr{L}/\delta\hat{\boldsymbol{u}} := 2\nabla^2\hat{\boldsymbol{u}} - b\left(\frac{dV}{dr} - \frac{V}{r}\right)\begin{pmatrix}\hat{v}\\ \hat{u}\\ 0\end{pmatrix} - \nabla p = 0, \quad (26)$$

$$\delta\mathscr{L}/\delta p := \nabla\cdot\hat{\boldsymbol{u}} = 0, \quad (27)$$

$$\delta\mathscr{L}/\delta V := \frac{d^2V}{dr^2} + \frac{1}{r}\frac{dV}{dr} - \frac{V}{r^2} - \frac{2(b-1)}{b}\left(\frac{d\overline{\hat{u}\hat{v}}}{dr} + \frac{2\overline{\hat{u}\hat{v}}}{r}\right) = 0, \quad (28)$$

$$\delta\mathscr{L}/\delta b := \frac{b^2-2b}{4(b-1)^2}\mathcal{I}_1 - \mathcal{I}_2 = 0, \quad (29)$$

where

$$\mathcal{I}_1 = \int_{r_i}^{r_o}\left\{r\left[\frac{d(V-V_{\rm lam})}{dr}\right]^2 + \frac{(V-V_{\rm lam})^2}{r}\right\}dr,$$

$$\mathcal{I}_2 = \int_{r_i}^{r_o}\overline{\hat{u}\hat{v}}\left(\frac{dV}{dr} - \frac{V}{r}\right)rdr.$$

When $\eta \to 1$ (small-gap limit), the Taylor-Couette flow approaches to the plane Couette flow. In this limit, the Euler-Lagrange equations (26)–(29) reduce to

$$2\nabla^2\hat{\boldsymbol{u}} - b\frac{dV}{dy}\begin{pmatrix}\hat{v}\\ \hat{u}\\ 0\end{pmatrix} - \nabla p = 0, \quad (30)$$

$$\nabla\cdot\hat{\boldsymbol{u}} = 0, \quad (31)$$

$$\frac{d^2V}{dy^2} - \frac{2(b-1)}{b}\frac{d\overline{\hat{u}\hat{v}}}{dy} = 0, \quad (32)$$

$$\frac{b^2-2b}{4(b-1)^2}\int_0^1\left(\frac{dV}{dy} - \mathrm{Re}\right)^2 dy - \int_0^1\overline{\hat{u}\hat{v}}\frac{dV}{dy}dy = 0, \quad (33)$$

where y is the wall-normal coordinate and the letters u and v here denote the streamwise and wall-normal velocity components, respectively. Equations (30)–(33) are equivalent to the Euler-Lagrange equations for plane Couette flow derived by Plasting and Kerswell [31] [refer to their Eqs. (2.13a)–(2.13d), although in a slightly different form from ours].

Note that Eqs. (26) and (27) are identical to the zero eigenvalue problem of the spectral constraint Eqs. (23) and (24). Generally, the solution of the Euler-Lagrange equations (26)–(29) is not unique. However, the solution satisfying the spectral constraint ($\lambda \leqslant 0$) is unique and delivers the best bound on ε [31,33]. The main challenge in solving the Euler-Lagrange equations is to satisfy the spectral constraint, which usually requires the Newton iteration with continuation method [31]. Typically, the Newton iteration requires a bifurcation analysis of the spectral constraint, which becomes tedious when considering a finite computational domain [32,33]. In contrast, the pseudo-time-stepping method recently proposed by Wen *et al.* [32,33] is easy to implement and requires no bifurcation analysis. It is thus adopted in the present paper. In the following section, we introduce the time-stepping system for our problem and the numerical method employed to solve it. Furthermore, we show that, if this numerical approach converges to a steady state, it is the global optimal.

V. NUMERICAL TECHNIQUE

A. Time-stepping system

The pseudo-time-stepping method converts the "time-invariant" Euler-Lagrange equations (26)–(28) into a time-dependent dynamical system [32,33], namely,

$$\frac{\partial\hat{\boldsymbol{u}}}{\partial t_1} = 2\nabla^2\hat{\boldsymbol{u}} - b\left(\frac{\partial V}{\partial r} - \frac{V}{r}\right)\begin{pmatrix}\hat{v}\\ \hat{u}\\ 0\end{pmatrix} - \nabla p, \quad (34)$$

$$\nabla\cdot\hat{\boldsymbol{u}} = 0, \quad (35)$$

$$\frac{\partial V}{\partial t_2} = \frac{\partial^2V}{\partial r^2} + \frac{1}{r}\frac{\partial V}{\partial r} - \frac{V}{r^2} - \frac{2(b-1)}{b}\left(\frac{\partial\overline{\hat{u}\hat{v}}}{\partial r} + \frac{2\overline{\hat{u}\hat{v}}}{r}\right). \quad (36)$$

In practice, the optimal condition Eq. (29) is also converted into a time-dependent version:

$$\frac{db}{dt_3} = \frac{b^2-2b}{4(b-1)^2}\mathcal{I}_1 - \mathcal{I}_2. \quad (37)$$

The steady solution of the time-stepping system corresponds to the solution of the "time-independent" Euler-Lagrange equations. Note that we used three different times t_i ($i = 1, 2, 3$) for the fluctuation field, the background field, and the balance parameter. Typically, the time step for the background field should be small due to the boundary layer structure near the walls. In Wen *et al.* [33], the same time step is used for all the equations, which slows down the time marching method considerably, especially at large Taylor numbers. Here, we allowed the time steps for the fluctuation field and for the balance parameter to be much larger than that for the background field, i.e., $t_1 = t_3 = 100t_2$. As a result, the spurious modes damp 100 times faster than in the original time-stepping method, which gives rise to significant computational savings. This expedient made it possible to perform the simulations at high Ta, which would have otherwise been prohibitively expensive.

The optimal solution has no azimuthal variation, i.e., all the terms with ∂_θ are zero (we also show numerical evidence of this in Fig. 9 of Appendix B):

$$\hat{\boldsymbol{u}} = \sum_{n=1}^{M}\begin{pmatrix}\hat{u}_n(r)\cos(k_nz)\\ \hat{v}_n(r)\cos(k_nz)\\ \hat{w}_n(r)\sin(k_nz)\end{pmatrix}, \quad p = \sum_{n=1}^{N}\hat{p}_n\cos(k_nz), \quad (38)$$

where n is the mode number, M is the finite truncation mode number, and $k_n{=}n\alpha$ is the wave number. The fundamental wave number is $\alpha = 2\pi/\Gamma$, where Γ is the axial length (or aspect ratio) of the computational domain, which is fixed in the present paper, as in Wen *et al.* [32,33]. To solve the time-stepping system, the Adams-Bashforth-Crank-Nicolson method is used. Chebyshev collocation method is employed for the spatial discretization [33]. As the Taylor number increases, the number of Chebyshev collocation points is increased from 30 to 250. The simulations are performed for a discrete set of $\mathrm{Ta}_i = 10^4 \times 10^{(i-1)/4}$ ranging from $\mathrm{Ta} = 10^3$ to 10^9, such that the data are uniformly distributed on a log-scale plot.

B. Steady state: The global optimal

In the following we prove that the steady state of the time-stepping system Eqs. (34)–(37) is the "global" optimal, i.e., the true solution of the Euler-Lagrange equations (26)–(29). For a fixed balance parameter b, assuming that a steady state $(\hat{\boldsymbol{u}}, V)$ is obtained, a perturbation $(\hat{\boldsymbol{u}}', V')$ is added onto this steady state. After linearizing, we obtain

$$\frac{\partial \hat{\boldsymbol{u}}'}{\partial t_1} = 2\nabla^2 \hat{\boldsymbol{u}}' - b\left(\frac{\partial V}{\partial r} - \frac{V}{r}\right)\begin{pmatrix}\hat{v}'\\ \hat{u}'\\ 0\end{pmatrix} - b\left(\frac{\partial V'}{\partial r} - \frac{V'}{r}\right)\begin{pmatrix}\hat{v}\\ \hat{u}\\ 0\end{pmatrix} - \nabla p', \tag{39}$$

$$\nabla \cdot \hat{\boldsymbol{u}}' = 0, \tag{40}$$

$$\frac{\partial V'}{\partial t_2} = \frac{\partial^2 V'}{\partial r^2} + \frac{1}{r}\frac{\partial V'}{\partial r} - \frac{V'}{r^2} - \frac{2(b-1)}{b}\left(\frac{\partial \overline{\hat{u}'\hat{v} + \hat{u}\hat{v}'}}{\partial r} + \frac{2\overline{\hat{u}'\hat{v} + \hat{u}\hat{v}'}}{r}\right). \tag{41}$$

Adding up $\hat{\boldsymbol{u}}'\cdot$ Eq. (39) and $\frac{b^2}{2(b-1)}V'\times$ Eq. (41) and using the continuity condition Eq. (40), we obtain

$$\frac{1}{2}\frac{\partial}{\partial t_1}\int_{\mathscr{V}} |\hat{\boldsymbol{u}}'|^2 d\mathscr{V} + \frac{1}{2}\frac{\partial}{\partial t_2}\int_{\mathscr{V}} \frac{b^2}{2(b-1)} V'^2 d\mathscr{V} = \underbrace{-\frac{b^2}{2(b-1)}\int_{\mathscr{V}}\left[\left(\frac{\partial V'}{\partial r}\right)^2 + \left(\frac{V'}{r}\right)^2\right] d\mathscr{V}}_{\leqslant 0} \underbrace{- 2\int_{\mathscr{V}} |\nabla \hat{\boldsymbol{u}}'|^2 + b\hat{u}'\hat{v}'\left(\frac{\partial V}{\partial r} - \frac{V}{r}\right) d\mathscr{V}}_{\mathscr{H}}, \tag{42}$$

where $\mathscr{V}$ is the volume of the computational domain.

If the background field V does not satisfy the spectral constraint, there should be some Fourier mode $\hat{\boldsymbol{u}}'$ which grows with time, such that no steady solution of Eq. (34) can be obtained (this is because the eigenvalue $\lambda > 0$). Hence, the steady state means that the background velocity field V satisfies the spectral constraint. In this case, there are four types of disturbances. The first type is $V' = 0$ and $\hat{\boldsymbol{u}}'$ is expanded by spurious modes ($\lambda < 0$), and the second type is $V' \neq 0$ and $\hat{\boldsymbol{u}}'$ is expanded by spurious modes. The third type is $V' \neq 0$ and $\hat{\boldsymbol{u}}'$ is expanded by the critical modes ($\lambda = 0$), and the fourth type is $V' = 0$ and $\hat{\boldsymbol{u}}'$ is expanded by the critical modes. For the first and second types of disturbances, because $\mathscr{H} > 0$ ($\lambda < 0$), the disturbance always decays with time, which indicates that spurious modes cannot be attractors. For the third type of disturbance, because $V' \neq 0$ and $\mathscr{H} = 0$, a strictly monotonic decay of the functional on the left-hand side of Eq. (42) is seen, and the disturbance will also decay in time. For the fourth type of disturbance, i.e., $V' = 0$ and $\mathscr{H} = 0$, the strictly monotonic decay of the functional on the left-hand side of Eq. (42) is lost. However, $V' = 0$ cannot persist because, in Eq. (41), the term

$$\frac{\partial \overline{\hat{u}'\hat{v} + \hat{u}\hat{v}'}}{\partial r} + \frac{2\overline{\hat{u}'\hat{v} + \hat{u}\hat{v}'}}{r} \neq 0.$$

Therefore, the first term on the right-hand side of Eq. (42) is negative at some instant in time (actually, if $V' = 0$ at the initial stage, V' starts to grow immediately when the system is perturbed by such disturbances) and the disturbances, therefore, decay. Hence, we can conclude that the noncritical modes ("spurious" or "local" optimal solutions) could never be attractors. Furthermore, if a steady state is obtained, it is the global optimal. However, this method does not guarantee the existence of a steady state, despite the successful numerical outcomes of this paper. Importantly, to obtain a global optimal, it is crucial that a nonzero initial condition for "enough modes" should be seeded to the time-stepping system to ensure that all critical modes can be found by the time-stepping method.

VI. RESULTS AND DISCUSSION

To compare our paper with the previous numerical simulations of a fixed outer cylinder case [16–19], throughout the rest of the paper we focus on the case of a fixed outer cylinder ($\mathrm{Re}_o = 0$). In this case the Taylor number is connected to the Reynolds number Re_i via $\mathrm{Ta} = \frac{(1+\eta)^6}{64\eta^4}\mathrm{Re}_i^2$. Results are presented for three typical values of the radius ratio, i.e., $\eta = 0.5$, 0.714, and 0.909, which have been extensively investigated experimentally and numerically [15–17,19]. Moreover, in order to analyze the small-gap limit ($\eta \to 1$) in which the Taylor-Couette flow approaches the plane-Couette flow, we also consider $\eta = 0.99$. In the following, we first analyze the energy stability point as a function of η.

A. Energy stability

The Taylor-Couette flow is linearly unstable due to the centrifugal force when the inner cylinder is rotating and the outer cylinder is fixed. The first bifurcation of the spectral constraint ($\lambda = 0$) should occur at the energy stability point [26,27,31]. The energy stability requires

$$\frac{dE}{dt} = -\int_{\mathscr{V}}\left[\left(\frac{dV_{\mathrm{lam}}}{dr} - \frac{V_{\mathrm{lam}}}{r}\right)u'v' + |\nabla \boldsymbol{u}'|^2\right] d\mathscr{V} \leqslant 0, \tag{43}$$

where $E = \int_{\mathscr{V}} \boldsymbol{u}'^2/2 d\mathscr{V}$ is the kinetic energy. Clearly, the right-hand side of Eq. (43) has the same form as the quadratic term $\mathscr{H}$ in Eq. (21) with $V = V_{\mathrm{lam}}$ and $b = 1$. As the Taylor number increases, the background field V starts to deviate from the laminar profile to satisfy the spectral constraint.

Figure 1 shows the critical value $\mathrm{Re}_{\mathrm{IC}}$ of the inner-cylinder Reynolds number and the critical wave number α_c obtained from the energy stability analysis as a function of the radius ratio η. In the limit $\eta \to 1$, $\mathrm{Re}_{\mathrm{IC}} = 82.56$ and $\alpha_c \approx 3.12$, which are in excellent agreement with the study by Plasting and Kerswell [31] for plane-Couette flow. Following Wen *et al.* [33], we fix the aspect ratio at $\Gamma = 2\pi/\alpha_c$, where α_c is the critical wave number predicted by the energy stability analysis. Therefore, for the three typical cases considered herein, $\eta = 0.5$, 0.714, and 0.909, we

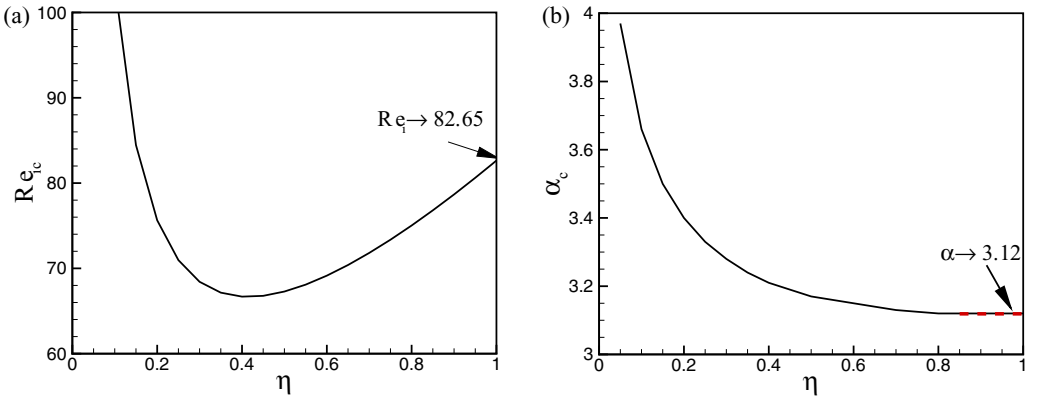

FIG. 1. (a) The critical value $\mathrm{Re}_{\mathrm{IC}}$ of the inner-cylinder Reynolds number vs the ratio η. (b) The critical wave number α_c vs the ratio η. The outer cylinder is fixed, $\mathrm{Re}_o = 0$.

obtain $\Gamma \approx 1.98,\ 2.00,$ and 2.01, respectively. Direct numerical simulations of Taylor-Couette flow with radius ratios $\eta = 0.5$ and 0.714 suggest that the optimal aspect ratio at high Taylor numbers is $\Gamma = 2$ [14,15,18,19]. For $\eta = 0.909$, the torque seems to be insensitive to Γ when $\Gamma > 2$ at high Taylor numbers $\mathrm{Ta} > 10^8$ [19]. Therefore, our data are available for comparison with those numerical studies [14,19] with aspect ratio $\Gamma \approx 2$.

B. Small gap

We consider $\eta = 0.99$ (small gap) and show that the time-stepping method can reproduce the results obtained by Plasting and Kerswell [31] in a much more efficient way. Here, we consider a fixed, relatively long domain $\Gamma = 10$, while Plasting and Kerswell considered an infinitely long domain. However, our results suggest that the upper bound

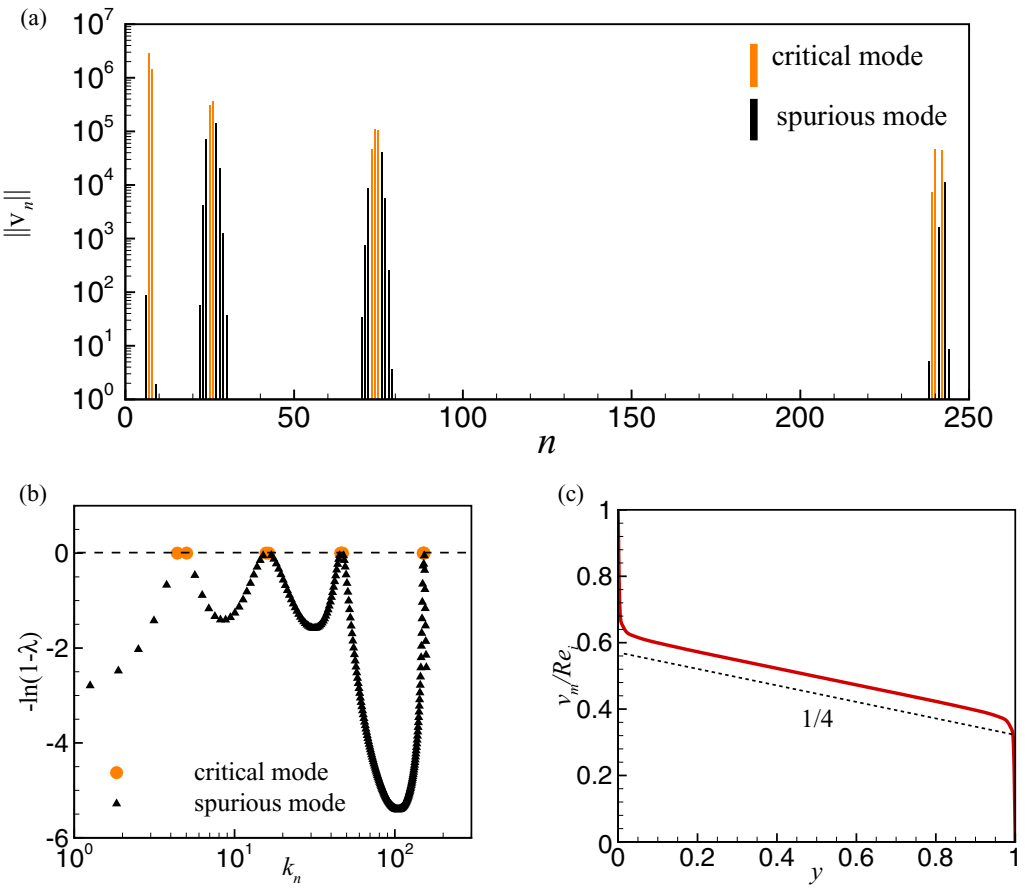

FIG. 2. (a) Norm of each mode of $\hat{v}$, $\|v_n\| = \frac{2}{r_o^2 - r_i^2} \int_{r_i}^{r_o} r v_n^2 dr$, at $t_1 = 4$, $\Delta t_1 = 10^{-5}$. There are still some undamped spurious modes. (b) Illustration of eigenvalues of the spectral constraint on a shifted logarithmic scale. (c) The mean velocity profile v_m plotted using a wall-normal coordinate $y = (r - r_i)/(r_o - r_i)$. (b), (c) All spurious modes are damped.

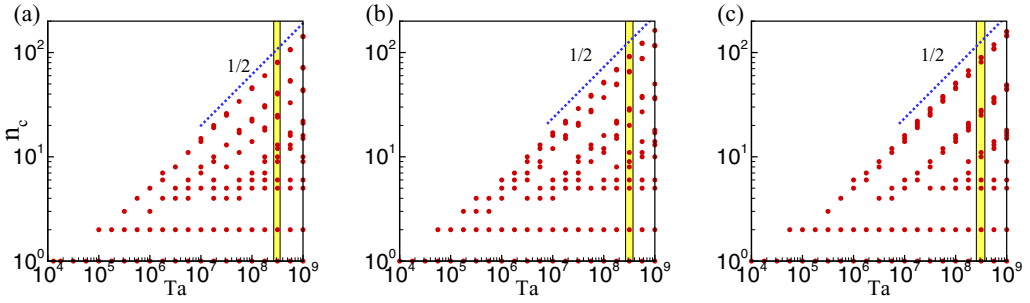

FIG. 3. The bifurcation diagram of the mode number n_c vs the Taylor number. (a) $\eta = 0.5$, $\alpha = 3.17$. (b) $\eta = 0.714$, $\alpha = 3.13$. (c) $\eta = 0.909$, $\alpha = 3.12$. The shaded modes are used to construct the optimal perturbation field in Fig. 4.

is insensitive to the domain size. The Reynolds numbers are fixed at $\mathrm{Re}_i = 10^4$ and $\mathrm{Re}_o = 0$. We used 300 nonzero modes as the initial condition for the time-stepping system (34)–(37). Most spurious modes are damped at $t_1 = 4$, as shown in Fig. 2(a). As in Wen *et al.* [33], we used a Newton iteration to improve the accuracy of the result and checked that the spectral constraint is satisfied, as demonstrated in Fig. 2(b). It is interesting that our discrete critical wave numbers $n_c\alpha$ are clustered around the four optimal wave numbers predicted by Plasting and Kerswell [31] (refer to their Fig. 3): $k_1 \approx 4.60$, $k_2 \approx 16.05$, $k_3 \approx 45.78$, and $k_4 \approx 150.09$. The rescaled viscous dissipation rate $\varepsilon/\mathrm{Re}_i^3$=0.00861 obtained from the time-stepping method also coincides with the results of Plasting and Kerswell [31] (refer to their Fig. 2). As shown in Fig. 2(c), the mean velocity profile exhibits a $1/4\mathrm{Re}_i$ slope in the interior region, a scaling that has been found in [31].

Plasting and Kerswell [31] used a Newton method in conjunction with a continuation method, which requires a bifurcation analysis of the spectral constraint. The time-stepping method, instead, requires no bifurcation analysis, and thus no continuation tool is needed. Clearly, an advantage of this is that, while in the continuation method the data at smaller Ta need to be available to continue the solution to higher Ta, the time-stepping method, instead, can be started at any Taylor number. When the domain size is fixed, the bifurcation analysis of Plasting and Kerswell [31] becomes very tedious since the critical wave numbers are discrete, which makes the parametric continuation very difficult.

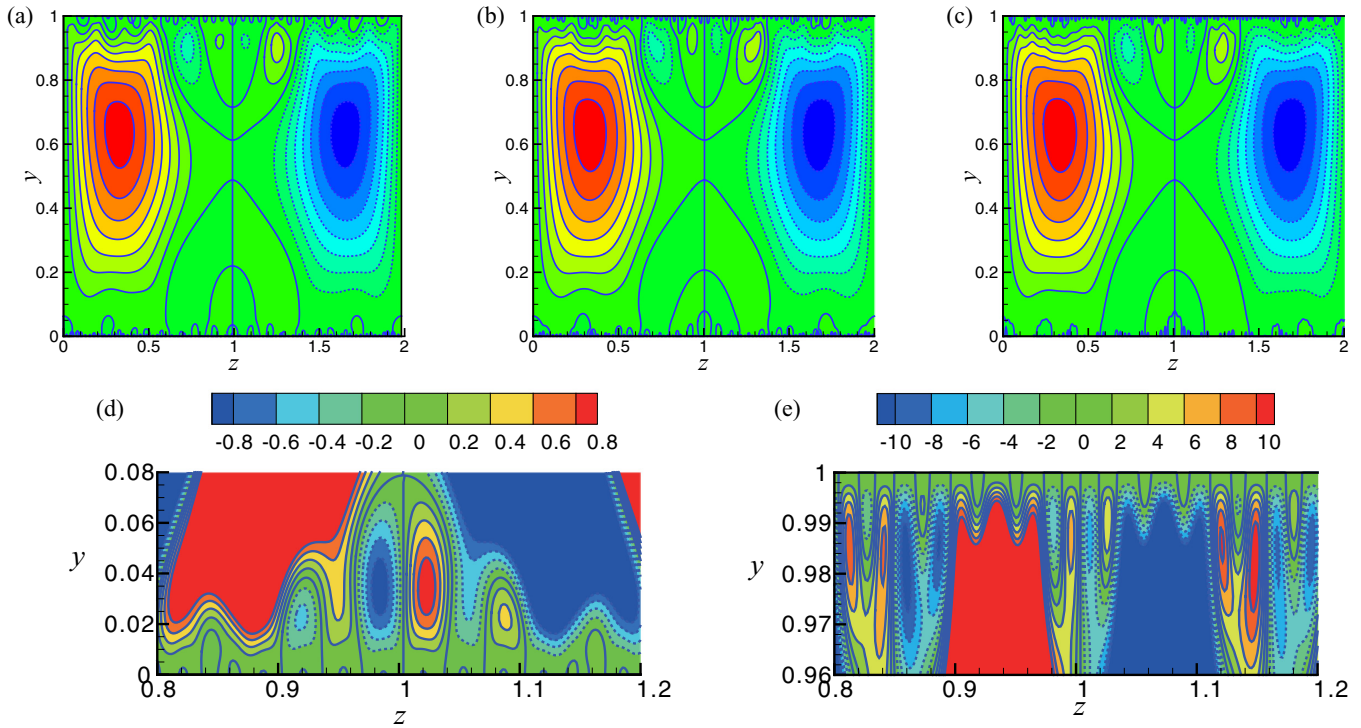

FIG. 4. (a)–(c) The optimal perturbation flow field in the y-z plane (y is the wall-normal coordinate defined in the caption of Fig. 2) for $\eta = 0.5,\ 0.714,$ and 0.909 at $\mathrm{Ta} = 316,\ 227,$ and 766, respectively. Here, to show the flow field, we introduce a stream function ψ such that $(\hat{u}, \hat{w}) = (\frac{1}{r}\frac{\partial\psi}{\partial z}, -\frac{1}{r}\frac{\partial\psi}{\partial z})$. The contour lines are plotted every $\Delta\psi = 50$ steps from $\psi = -280$ to 280 (solid lines are for positive ψ and dashed lines are for negative ψ). (d), (e) The near wall flow field of $\eta = 0.714$, showing that the small scale motion near the outer cylinder is more vigorous.

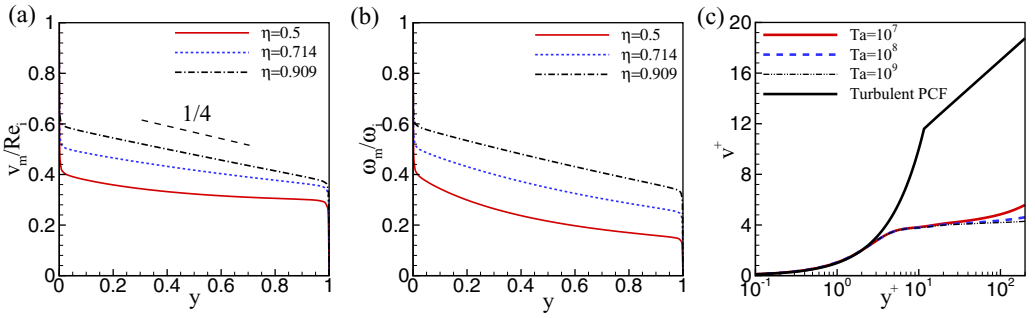

FIG. 5. (a), (b) The rescaled mean velocity profiles and mean angular velocity profiles at $\mathrm{Ta} = 10^9$. (c) The comparison between the optimal mean velocity profile at $\eta = 0.909$ and the mean velocity profile of fully developed turbulent plane Couette flow (PCF): A viscous sublayer $v^+ = y^+$ and a logarithmic region $v^+ = 2.5\ln(y^+) + 5.5$. Here $y^+ = \mathrm{Re}_\tau y$ and $v^+ = v_m/\mathrm{Re}_\tau$ with the friction Reynolds number $\mathrm{Re}_\tau = \sqrt{\varepsilon/\mathrm{Re}_i}$.

C. Upper bound on energy dissipation

We now consider the radius ratios $\eta = 0.5$, 0.714, and 0.909. The bifurcation diagrams of the critical modes n_c for these three cases are illustrated in Fig. 3. More critical modes are found to emerge as the Taylor number increases. The largest wave number $n_{\max}$ in Fig. 3 scales as $\mathrm{Ta}^{1/2}$. A close look at Fig. 3 reveals that the low wave numbers $n = 1$, 2, 5, and 6 at high Ta ($\mathrm{Ta} > 10^8$) are not sensitive to the geometry, i.e., to the radius ratio. However, high wave numbers are quite sensitive to the geometry, e.g., the largest critical wave number $n = 81$ for $\eta = 0.5$ and $n = 92$ for $\eta = 0.714$. This suggests that large structures of the optimal fields for $\eta = 0.5$, 0.714, and 0.909 are quite similar, while small structures can be quite different, as illustrated in Fig. 4. It is also interesting that the optimal small-scale motion near the outer cylinder is more vigorous than that near the inner cylinder.

Figure 5(a) displays the optimal mean profiles of azimuthal velocity v_m at $\mathrm{Ta} = 10^9$ for different radius ratios. The mean azimuthal velocity significantly depends on η and the boundary layer thins as η increases. For $\eta = 0.909$, the slope of v_m in the interior region is close to $\frac{1}{4}\mathrm{Re}_i$ [31]. This suggests that the gap is already small at $\eta = 0.909$, i.e., the Taylor-Couette flow mimics the plane-Couette flow. The rescaled mean angular velocity profiles $\omega_m = v_m/r$ for $\eta = 0.5$ and 0.714 shown in Fig. 5(b) share many features exhibited by the mean angular velocity profiles from DNS [17,19]. For example, Ostilla-Mónico *et al.* [19] showed that the gradient of the averaged angular velocity profile in the turbulent bulk region is around 0.25 at $\eta = 0.714$, which is close to the present result. However, for $\eta = 0.909$, Ostilla-Mónico *et al.* showed that the ω_m is flat in the interior part, which is very different from the present paper. Figure 5(c) shows a comparison of the optimal mean velocity profile at $\eta = 0.909$ with the empirically observed mean velocity profile for turbulent plane Couette flow. The mean velocity profile is significantly different from the empirical logarithmic velocity profile, indicating that the optimal velocity profile can only capture the dynamics in the viscous sublayer, when the gap is small. This suggests that the one-dimensional background approach loses important dynamical information of the system. We will examine in Sec. VII if a three-dimensional background approach can improve the bound by incorporating all dynamical information of the system, especially the momentum equation.

We assume the power-law ansatz $\mathrm{Nu} \leqslant c\mathrm{Ta}^\beta$. The power-law exponent is calculated using a backward finite difference method:

$$\beta_i = \frac{\log_{10}\mathrm{Nu}_{i+1} - \log_{10}\mathrm{Nu}_i}{\log_{10}\mathrm{Ta}_{i+1} - \log_{10}\mathrm{Ta}_i}. \tag{44}$$

Here Nu_i is the Nusselt number at Ta_i. Results in Fig. 6 demonstrate that the power-law exponent β approaches 1/2 asymptotically as Ta increases (we also show a rigorous proof of this in Appendix A). Results in Fig. 7(a) show that the upper bound on angular momentum transport scales as $\mathrm{Ta}^{1/2}$ in the asymptotic ultimate regime. The prefactor c is also shown in Fig. 7(b). Using the power-law ansatz, for the fixed outer cylinder ($\mathrm{Re}_o \equiv 0$), it is found that the energy dissipation rate

$$\varepsilon \leqslant c\mathrm{Pr}^{-2}\mathrm{Ta}^{3/2} = \frac{c(1+\eta)}{2\eta^2}\mathrm{Re}_i^3, \tag{45}$$

which reduces to $\varepsilon \lesssim c\mathrm{Re}_i^3$ as $\eta \to 1$. For a fixed outer cylinder and under the small gap assumption, Doering and Constantin [25] derived a rigorous upper bound on torque (or Nusselt number) $\varepsilon \lesssim 0.0885\mathrm{Re}_i^3$. In the present paper, for the case $\eta = 0.909$, we have $\varepsilon \leqslant 0.0085\mathrm{Re}_i^3$, which is an order of magnitude lower than Doering and Constantin's rigorous bound. Constantin [30] considered the curvature effect and showed a rigorous upper bound on energy dissipation rate in Taylor-Couette flow, $\varepsilon \leqslant \frac{2\eta^2}{1-\eta^2}\mathrm{Re}_i^3$, which gives

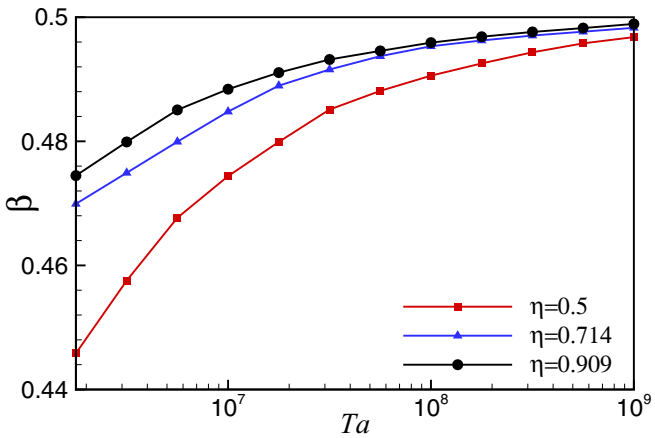

FIG. 6. The power-law exponent β vs the Taylor number Ta.

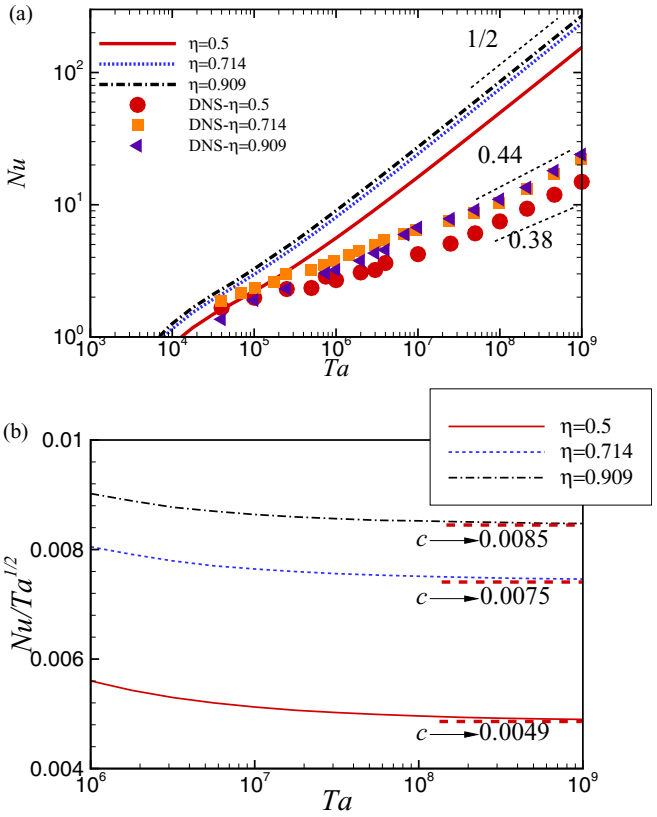

FIG. 7. (a) The upper bound of Nussult number Nu vs the Taylor number Ta. Symbols are DNS, courtesy of Dr. Rodolfo Ostilla-Mónico. (b) A plot of $\mathrm{Nu}/\mathrm{Ta}^{1/2}$ vs the Taylor number Ta.

$\varepsilon \leqslant 0.3333\mathrm{Re}^3$ for $\eta = 0.5$ and $\varepsilon \leqslant 2.0799\mathrm{Re}_i^3$ for $\eta = 0.714$. Here, we are able to lower these bounds by up to two orders of magnitudes, i.e., $\varepsilon \leqslant 0.0147\mathrm{Re}^3$ for $\eta = 0.5$ and $\varepsilon \leqslant 0.0126\mathrm{Re}_i^3$ for $\eta = 0.714$. Our results thus significantly improve the rigorous upper bounds derived by Doering and Constantin [25] and Constantin [30].

Plasting and Kerswell [31] have shown that the optimal balance parameter approaches 3/2 in the plane-Couette flow. Figure 8 shows that $b \to 3/2$ for all the three radius ratios considered, thus demonstrating that the optimal balance parameter is independent of the geometry.

In the ultimate regime, previous numerical and experimental studies [4–6,14–19] suggest that the power-law exponent is between 0.38 and 0.44 [see Fig. 7(a)]. The power-law exponent $\beta = 1/2$ obtained in the present paper is higher

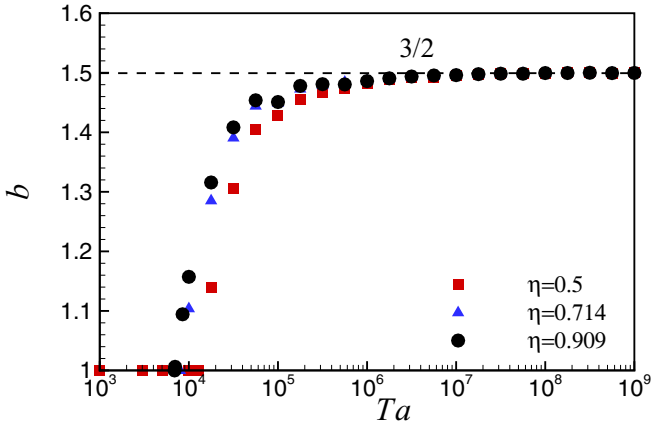

FIG. 8. The optimal balance parameter vs the Taylor number Ta.

than these experimental and numerical data. It is clear that the one-dimensional background approach has not exhausted all the dynamical information of the equations, especially the momentum equation. Therefore, the one-dimensional background approach produces a higher scaling on the angular momentum transport than the DNS data. However, it is still unclear whether the "steady" solutions of the Navier-Stokes equations can produce bounds on the angular momentum transport or not. Moreover, another question is the following: Can we reduce the bound of $\mathrm{Nu} \leqslant c\mathrm{Ta}^{1/2}$ by considering a three-dimensional steady background field? We are going to examine these issues in the following section.

VII. THREE-DIMENSIONAL BACKGROUND FIELD

In this section we revisit the upper-bound variational problem to understand if a three-dimensional background field can improve the bound on ε. The analysis is carried out on the plane-Couette flow for simplicity, as it was shown above that the Taylor-Couette flow mimics the plane-Couette flow when the gap is small. To maximize the viscous dissipation rate $\varepsilon = \langle|\nabla \boldsymbol{u}|^2\rangle$, the following Lagrangian is constructed:

$$\mathfrak{L} = \langle|\nabla \boldsymbol{u}|^2\rangle - a\langle \boldsymbol{u}' \cdot \boldsymbol{\mathcal{N}}\rangle, \tag{46}$$

where $\boldsymbol{u} = \boldsymbol{u}_b + \boldsymbol{u}'$. Here, we consider a three-dimensional background flow $\boldsymbol{u}_b(x, y, z)$, where x, y, and z are the streamwise, wall-normal, and spanwise directions, respectively. Since we are considering a steady background field, the Lagrangian (46) imposes the steady or infinitely long time-averaged momentum equation as a constraint. Integration by parts of Eq. (46) gives

$$\mathfrak{L} = \langle|\nabla \boldsymbol{u}_b|^2\rangle - \underbrace{\langle(a-1)|\nabla \boldsymbol{u}'|^2 + a\boldsymbol{u}' \cdot \nabla \boldsymbol{u}_b \cdot \boldsymbol{u}' + a\boldsymbol{u}_b \cdot \nabla \boldsymbol{u}_b \cdot \boldsymbol{u}' - (a-2)\boldsymbol{u}' \cdot \nabla^2 \boldsymbol{u}_b\rangle}_{\mathscr{G}}. \tag{47}$$

Therefore, the upper bound on the energy dissipation is given by

$$\varepsilon \leqslant \langle|\nabla \boldsymbol{u}_b|^2\rangle - \inf \mathscr{G}, \tag{48}$$

provided $a > 1$. The chosen background field $\boldsymbol{u}_b$ should ensure the existence of $\inf \mathscr{G}$. The minimum of $\mathscr{G}$ can be sought by solving the following Euler-Lagrange system by fixing $\boldsymbol{u}_b$ and a [28]:

$$\boldsymbol{\nabla} \cdot \boldsymbol{u}' = 0, \tag{49}$$

$$-2(a-1)\nabla^2 \boldsymbol{u}' + a\left(\boldsymbol{\nabla}\boldsymbol{u}_b + \boldsymbol{\nabla}\boldsymbol{u}_b^T\right) \cdot \boldsymbol{u}' + \boldsymbol{\nabla} p = (a-2)\nabla^2 \boldsymbol{u}_b - a\boldsymbol{u}_b \cdot \boldsymbol{\nabla}\boldsymbol{u}_b. \tag{50}$$

The solution of $\boldsymbol{u}'$ to the above equation is denoted as $\boldsymbol{u}_0$.

Following Ding and Kerswell [35], to minimize the bound in Eq. (48) subject to the spectral constraint and mass conservation, we write the following Lagrangian:

$$L = \langle |\boldsymbol{\nabla}\boldsymbol{u}_b|^2 \rangle - \mathscr{G}(\boldsymbol{u}_0, \boldsymbol{u}_b, a) - \sum_{i=1}^{N} \underbrace{\langle (a-1)|\boldsymbol{\nabla}\boldsymbol{u}_i|^2 + a\boldsymbol{u}_i \cdot \boldsymbol{\nabla}\boldsymbol{u}_b \cdot \boldsymbol{u}_i \rangle}_{\mathscr{H}_i} + \langle p_i \boldsymbol{\nabla} \cdot \boldsymbol{u}_i \rangle \tag{51}$$

where $\mathscr{H}_i(\boldsymbol{u}_i, \boldsymbol{u}_b, a)$ is a quadratic form which must be positive semidefinite (the spectral constraint) for $\inf \mathscr{G}$ to exist. The Lagrangian (51) is to ensure that, when a new mode becomes marginal in the spectral constraint as Re increases, this new mode is pinned at the ground state $\lambda = 0$, so that it remains marginal. When $\boldsymbol{u}_b$ is one dimensional and we decompose $\boldsymbol{u}_i$ in Fourier modes $\boldsymbol{u}_i = \hat{\boldsymbol{u}}_i \exp(I\boldsymbol{k}_i \cdot \boldsymbol{x})$ [here $I = \sqrt{-1}$, $\boldsymbol{k}_i = (k_{ix}, k_{iz})$ $\boldsymbol{x} = (x, z)$], due to the natural orthogonality property of different marginal fluctuation fields, the following relation holds:

$$\sum_{i=1}^{N} \mathscr{H}_i = \mathscr{H} = \langle (a-1)|\boldsymbol{\nabla}\boldsymbol{u}'|^2 + a\boldsymbol{u}' \cdot \boldsymbol{\nabla}\boldsymbol{u}_b \cdot \boldsymbol{u}' \rangle, \tag{52}$$

where $\boldsymbol{u}' = \sum_{i=1}^{N} \boldsymbol{u}_i$. When a new spectrally marginal mode appears, the "pinning" is done by simply extending the set of wave numbers contributing to the definition of the fluctuation field by one. However, when $\boldsymbol{u}_b$ is three dimensional, the equality in (52) does not hold any more because there is more than one marginal mode for a given wave number $\boldsymbol{k}_i$ (see chapter 3 in [34]). In these scenarios, the natural orthogonality property of different marginal fluctuation fields disappears, implying that the physical meaning of the fluctuation fields is lost, i.e., the fluctuation field cannot be written as a linear superposition of the marginal fields. Hence, the Lagrangian (51) pins all marginal modes *separately* when $\boldsymbol{u}_b$ is three dimensional.

An interesting observation is that the spectral constraint is not satisfied for $N > 1$ at any saddle point of the Lagrangian (47), where the dynamical constraints from the steady momentum equation are imposed. Consequently, the optimization procedure is forced to find an optimal solution away from the saddle points of the Lagrangian (47) where the spectral constraint $\mathscr{H} \geqslant 0$ is satisfied to deliver a true bound [35]. The steady momentum equation is therefore not satisfied although it is explicitly imposed as a constraint in Eq. (46), which indicates that there is no direct connection between the optimal solution and the steady solution to the Navier-Stokes equations. Hence, the Lagrangian in (51) indicates that the scalings produced by *any* steady solutions of the Navier-Stokes equation are not bounds on the angular momentum transport because these solutions do not guarantee that the "spectral constraint" is satisfied (this is also suggested in Ding and Kerswell [35] for the Rayleigh-Bénard problem). Below, we shall focus on examining if the three-dimensional background field can lower the bound produced by the one-dimensional background field study.

At the bifurcation point $\mathrm{Re} = \mathrm{Re}_c = 82.65$, $\boldsymbol{u}_b = \mathrm{Re}_c y \boldsymbol{e}_x$, we have $a = \infty$ [31]. Therefore, we introduce $b = a/(a-1)$ and rewrite the Lagrangian (51) as

$$L = \langle |\boldsymbol{\nabla}\boldsymbol{u}_b|^2 \rangle - \left\langle \frac{1}{b-1}|\boldsymbol{\nabla}\boldsymbol{u}_0|^2 + \frac{b}{b-1}(\boldsymbol{u}_0 \cdot \boldsymbol{\nabla}\boldsymbol{u}_b \cdot \boldsymbol{u}_0 + \boldsymbol{u}_b \cdot \boldsymbol{\nabla}\boldsymbol{u}_b \cdot \boldsymbol{u}_0) - \frac{2-b}{b-1}\boldsymbol{u}_0 \cdot \nabla^2 \boldsymbol{u}_b \right\rangle + \langle p\boldsymbol{\nabla} \cdot \boldsymbol{u}_0 \rangle - \langle q\boldsymbol{\nabla} \cdot \boldsymbol{u}_b \rangle - \sum_{i=1}^{N} \underbrace{\langle |\boldsymbol{\nabla}\boldsymbol{u}_i|^2 + b\boldsymbol{u}_i \cdot \boldsymbol{\nabla}\boldsymbol{u}_b \cdot \boldsymbol{u}_i - p_i \boldsymbol{\nabla} \cdot \boldsymbol{u}_i \rangle}_{\mathscr{H}}, \tag{53}$$

where we rescale $\boldsymbol{u}_i/\sqrt{b-1} \to \boldsymbol{u}_i$ $(i = 1, 2, \ldots)$. Variation of the Lagrangian (53) leads to the Euler-Lagrange equations

$$\frac{\delta L}{\delta p_i} := \boldsymbol{\nabla} \cdot \boldsymbol{u}_i = 0, \tag{54}$$

$$\frac{\delta L}{\delta \boldsymbol{u}_i} := -2\nabla^2 \boldsymbol{u}_i + b\left(\boldsymbol{\nabla}\boldsymbol{u}_b + \boldsymbol{\nabla}\boldsymbol{u}_b^T\right) \cdot \boldsymbol{u}_i + \boldsymbol{\nabla} p_i - [(2-b)\nabla^2 \boldsymbol{u}_b - b\boldsymbol{u}_b \cdot \boldsymbol{\nabla}\boldsymbol{u}_b]\delta_{0i} = 0, \tag{55}$$

$$\frac{\delta L}{\delta q} := \boldsymbol{\nabla} \cdot \boldsymbol{u}_b = 0, \tag{56}$$

$$\frac{\delta L}{\delta \boldsymbol{u}_b} := -2\nabla^2 \boldsymbol{u}_b - \frac{b}{b-1}\left(\boldsymbol{\nabla}\boldsymbol{u}_b^T \cdot \boldsymbol{u}_0 - \boldsymbol{u}_b \cdot \boldsymbol{\nabla}\boldsymbol{u}_0 - \boldsymbol{u}_0 \cdot \boldsymbol{\nabla}\boldsymbol{u}_0\right) + \frac{2-b}{b-1}\nabla^2 \boldsymbol{u}_0 + \boldsymbol{\nabla} q + \sum_{i=1}^{N} b\boldsymbol{u}_i \cdot \boldsymbol{\nabla}\boldsymbol{u}_i = 0, \tag{57}$$

$$\frac{\delta L}{\delta b} := \langle |\boldsymbol{\nabla}\boldsymbol{u}_0|^2 + \boldsymbol{u}_0 \cdot \boldsymbol{\nabla}\boldsymbol{u}_b \cdot \boldsymbol{u}_0 + \boldsymbol{u}_b \cdot \boldsymbol{\nabla}\boldsymbol{u}_b \cdot \boldsymbol{u}_0 - \boldsymbol{u}_0 \cdot \nabla^2 \boldsymbol{u}_b \rangle + (b-1)^2 \sum_{i=1}^{N} \langle \boldsymbol{u}_i \cdot \boldsymbol{\nabla}\boldsymbol{u}_b \cdot \boldsymbol{u}_i \rangle = 0, \tag{58}$$

where δ_{0i} is the Kronecker delta. The solution at the first bifurcation point $\mathrm{Re} = \mathrm{Re}_c$ is $\boldsymbol{u}_b = \mathrm{Re}_c y \boldsymbol{e}_x$ and $\boldsymbol{u}_0 = \boldsymbol{0}$, $b = 1$.

A. First bifurcation

We slightly increase the critical Reynolds number by ϵ and expand the solutions asymptotically as follows:

$$\boldsymbol{u}_b = \mathrm{Re}_c y \boldsymbol{e}_x + \epsilon \delta \boldsymbol{u}_b + \ldots, \tag{59}$$

$$\boldsymbol{u}_0 = \epsilon \delta \boldsymbol{u}_0 + \ldots, \tag{60}$$

$$\boldsymbol{u}_i = \boldsymbol{u}_i^0 + \epsilon \boldsymbol{u}_i^1 + \ldots, \quad i \geqslant 1, \tag{61}$$

$$b = 1 + \epsilon b_1 + \ldots, \tag{62}$$

$$p_i = p_i^0 + \epsilon \delta p_i + \ldots, \tag{63}$$

$$q = q^0 + \epsilon \delta q + \ldots. \tag{64}$$

The leading order solution for fluctuation field $\boldsymbol{u}_i^0$ $(i \neq 0)$ is solved from the spectral constraint $\mathcal{L}(\boldsymbol{u}_i^0) = 0$ ($\mathcal{L}$ identifies the left-hand side of the two equations below):

$$\nabla \cdot \boldsymbol{u}_i^0 = 0, \tag{65}$$

$$-2\nabla^2 \boldsymbol{u}_i^0 + \left(\nabla \boldsymbol{u}_{b0} + \nabla \boldsymbol{u}_{b0}^T\right) \cdot \boldsymbol{u}_i^0 + \nabla p_i^0 = 0. \tag{66}$$

Here $\boldsymbol{u}_{b0} = \mathrm{Re}_c y \boldsymbol{e}_x$ is the leading order solution for the background field. The spectral constraint has the following two solutions:

$$\boldsymbol{u}_1^0 = AU(y)\cos(kz)\boldsymbol{e}_x + AV(y)\cos(kz)\boldsymbol{e}_y + AW(y)\sin(kz)\boldsymbol{e}_z, \tag{67}$$

$$\boldsymbol{u}_2^0 = -BU(y)\sin(kz)\boldsymbol{e}_x - BV(y)\sin(kz)\boldsymbol{e}_y + BW(y)\cos(kz)\boldsymbol{e}_z \tag{68}$$

where $(U, V, W)^T$ is the eigenvector and A and B are the amplitudes of the perturbation. When we consider a one-dimensional background flow field, the two modes are pinned simultaneously as we require either mode to satisfy the spectral constraint due to the symmetry in the spanwise direction, i.e., any phase shift of either mode does not change the spectral constraint. However, if the background flow is three dimensional, both modes should be pinned separately because the spanwise symmetry is lost [35].

The first order solution for the fluctuation field $\delta \boldsymbol{u}_0$ satisfies the following linear equations:

$$\nabla \cdot \delta \boldsymbol{u}_0 = 0, \tag{69}$$

$$\frac{1}{b_1}\nabla^2 \delta \boldsymbol{u}_0 + \frac{\mathrm{Re}_c}{b_1}(\delta u_0 \boldsymbol{e}_y + \delta v_0 \boldsymbol{e}_x) + \nabla \delta q + \sum_{i=1,2} \boldsymbol{u}_i^0 \cdot \nabla \boldsymbol{u}_i^0 = 0, \tag{70}$$

$$\delta \boldsymbol{u}_0 = 0, \quad y = \pm 1, \tag{71}$$

where Eq. (70) is obtained from the Euler-Lagrange equation (57). Evaluating the driving term $\sum_{i=1}^2 \boldsymbol{u}_i^0 \cdot \nabla \boldsymbol{u}_i^0$ gives

$$\sum_{i=1}^{2} \boldsymbol{u}_i^0 \cdot \nabla \boldsymbol{u}_i^0 = \frac{1}{2}(A^2 + B^2)\begin{pmatrix} U'V - kUW \\ VV' - kVW \\ 0 \end{pmatrix} + \frac{1}{2}(A^2 - B^2)\begin{pmatrix} (U'V + kUW)\cos(2kz) \\ (VV' + kWV)\cos(2kz) \\ (VW' + kWW)\sin(2kz) \end{pmatrix}. \tag{72}$$

The prime decoration denotes the wall-normal derivative. Note that the term $\frac{1}{2}(A^2 + B^2)(VV' - kVW)\boldsymbol{e}_y$ can be absorbed into the pressure. Therefore, the solution for $\delta \boldsymbol{u}_0$ can be written as

$$\delta \boldsymbol{u}_0 = (A^2 + B^2)F(y)\boldsymbol{e}_x + (A^2 - B^2)\boldsymbol{G} \tag{73}$$

where $\boldsymbol{G} = (G_1(y)\cos(2kz), G_2(y)\cos(2kz), G_3(y)\sin(2kz))^T$. $\boldsymbol{G}$ satisfies the mass conservative condition and the G_i $(i = 1, 2, 3)$ depend on the eigenvector $(U, V, W)^T$. Both F and $\boldsymbol{G}$ satisfy homogeneous boundary conditions.

The spectral constraint at $O(\epsilon)$ reads

$$\nabla \cdot \boldsymbol{u}_i^1 = 0, \tag{74}$$

$$-2\nabla^2 \boldsymbol{u}_i^1 + \left(\nabla \boldsymbol{u}_{b0} + \nabla \boldsymbol{u}_{b0}^T\right) \cdot \boldsymbol{u}_i^1 + \nabla \delta p_i = -b_1\left(\nabla \boldsymbol{u}_{b0} + \nabla \boldsymbol{u}_{b0}^T\right) \cdot \boldsymbol{u}_i^0 - \left(\nabla \delta \boldsymbol{u}_b + \nabla \delta \boldsymbol{u}_b^T\right) \cdot \boldsymbol{u}_i^0. \tag{75}$$

Since the operator $\mathcal{L}$ is self-adjoint and annihilates $\boldsymbol{u}_j^0$ [see Eqs. (65) and (66)], the following solvability condition of the first order spectral constraint arises:

$$\left\langle \boldsymbol{u}_j^0 \cdot \mathcal{L}(\boldsymbol{u}_i^1) \right\rangle = \left\langle \boldsymbol{u}_i^1 \cdot \mathcal{L}(\boldsymbol{u}_j^0) \right\rangle = 0, \tag{76}$$

which yields

$$\left\langle \boldsymbol{u}_i^0 \cdot \left[b_1\left(\nabla \boldsymbol{u}_{b0} + \nabla \boldsymbol{u}_{b0}^T\right) \cdot \boldsymbol{u}_i^0 + \left(\nabla \delta \boldsymbol{u}_b + \nabla \delta \boldsymbol{u}_b^T\right) \cdot \boldsymbol{u}_i^0 \right] \right\rangle = 0, \tag{77}$$

$$\left\langle \boldsymbol{u}_j^0 \cdot \left[b_1\left(\nabla \boldsymbol{u}_{b0} + \nabla \boldsymbol{u}_{b0}^T\right) \cdot \boldsymbol{u}_i^0 + \left(\nabla \delta \boldsymbol{u}_b + \nabla \delta \boldsymbol{u}_b^T\right) \cdot \boldsymbol{u}_i^0 \right] \right\rangle = 0, \quad i \neq j. \tag{78}$$

When $i \neq j$, the solvability condition is automatically satisfied because u_i^0 and u_j^0 are orthogonal.

Furthermore, the first order solution for the background field, $\delta \boldsymbol{u}_b$, is obtained by solving

$$\nabla \cdot \delta \boldsymbol{u}_b = 0, \tag{79}$$

$$\nabla^2 \delta \boldsymbol{u}_b - \delta \boldsymbol{u}_b \cdot \nabla \boldsymbol{u}_{b0} = -2\nabla^2 \delta \boldsymbol{u}_0 + \left(\nabla \boldsymbol{u}_{b0} + \nabla \boldsymbol{u}_{b0}^T\right) \cdot \delta \boldsymbol{u}_0 + \nabla \delta p_0. \tag{80}$$

Clearly, $\delta \boldsymbol{u}_b$ should have the same phase as $\delta \boldsymbol{u}_0$ and can also be written as

$$\delta \boldsymbol{u}_b = y\boldsymbol{e}_x + (A^2 + B^2)P(y)\boldsymbol{e}_x + (A^2 - B^2)\boldsymbol{Q} \tag{81}$$

where $\boldsymbol{Q} = (Q_1(y)\cos(2kz), Q_2(y)\cos(2kz), Q_3(y)\sin(2kz))$. $\boldsymbol{Q}$ satisfies the divergence free condition. Both P and $\boldsymbol{Q}$ satisfy the homogeneous boundary conditions at $y = \pm 1$. For $i = 1$ and 2, Eq. (77) gives

$$(1 + b_1 \mathrm{Re}_c)\int_{-1}^{1} UV dy + (A^2 + B^2)\int_0^1 P'UV dy = \pm(A^2 - B^2)\mathcal{J}, \tag{82}$$

where the plus and minus signs before $(A^2 - B^2)$ are chosen for $i = 1$ and 2, respectively, and $\mathcal{J} = \int_{-1}^{1}[-kUWQ_1 + \frac{1}{2}UVQ_1' + \frac{1}{2}VW(Q_3' - 2kQ_2) + \frac{1}{2}V^2Q_2' + kW^2Q_3]dy$. There is no free parameter in $\mathcal{J}$, which is generically nonzero such that one can determine the parameters b_1 and A^2 (or B^2) using Eqs. (58) and (82) (if $\mathcal{J} = 0$, the solvability conditions are linearly dependent, and we are left with two equations to determine three unknowns, which is impossible. However, we are unable to prove $\mathcal{J} \neq 0$ always holds although numerics suggests so, like in Ding and Kerswell [35]). Therefore, the solvability condition (77) forces the two modes to choose the same amplitude, i.e.,

$A^2 = B^2$, and $\delta \boldsymbol{u}_b$ collapses to a one-dimensional profile. This asymptotic analysis can be applied as Re is increased provided that no new modes arise; then $A^2 = B^2$ always holds such that the optimal background field remains one-dimensional.

B. Subsequent bifurcations

We assume that the background velocity field $\boldsymbol{u}_b$ remains one-dimensional after mth bifurcation and there are m different wave numbers. We are going to show that at $(m+1)$th bifurcation it still remains one-dimensional. The leading order solutions of the spectral constraint at the $(m+1)$th bifurcation point can be written as

$$\boldsymbol{u}^0_{2i-1} = A_i(U_i \cos(k_i z), V_i \cos(k_i z), W_i \sin(k_i z))^T, \tag{83}$$

$$\boldsymbol{u}^0_{2i} = B_i(-U_i \sin(k_i y), -V_i \sin(k_i y), W_i \cos(k_i y))^T \tag{84}$$

where $A_i^2 = B_i^2$ for $i = 1, 2, \ldots, m$. We are aiming at proving that $A^2_{m+1} = B^2_{m+1}$ at the $(m+1)$th bifurcation point.

We assume that the Reynolds number is increased by $\mathrm{Re} = \mathrm{Re}_{m+1} + \epsilon$ at the $(m+1)$th bifurcation point and we expand the variables asymptotically:

$$\boldsymbol{u}_b = \mathcal{U}(y)\boldsymbol{e}_x + \epsilon \delta \boldsymbol{u}_b + \ldots, \tag{85}$$

$$\boldsymbol{u}_0 = u_0(y)\boldsymbol{e}_x + \epsilon \delta \boldsymbol{u}_0 + \ldots, \tag{86}$$

$$\boldsymbol{u}_i = \begin{cases} \boldsymbol{u}_i^0 + \epsilon \boldsymbol{u}_i^1 + \ldots, & i = 1, 2, \ldots, 2m, \\ \epsilon^{1/2}\boldsymbol{u}_i^0 + \epsilon^{3/2}\boldsymbol{u}_i^1 + \ldots, & i = 2m+1, 2m+2, \end{cases} \tag{87}$$

$$b = b_0 + \epsilon b_1 + \ldots., \tag{88}$$

$$p_i = p_i^0 + \epsilon \delta p_i + \ldots, \tag{89}$$

$$q = q^0 + \epsilon \delta q + \ldots. \tag{90}$$

Here, because the nonlinear interaction of the two new modes is of order $O(\epsilon)$, i.e., $\boldsymbol{u}_i^0 \cdot \nabla \boldsymbol{u}_i^0 = O(\epsilon)$ $(i = 2m+1,\ 2m+2)$, the amplitude of the $\boldsymbol{u}_i^0$ is of order $O(\epsilon^{1/2})$. Therefore $\boldsymbol{u}_i$ $(i = 2m+1,\ 2m+2)$ is expanded in a fractional power series of ϵ. The first order equations for $\delta \boldsymbol{u}_0$ and $\delta \boldsymbol{u}_b$ are

$$\begin{aligned} &-2\nabla^2 \delta \boldsymbol{u}_0 + b_0(\mathcal{U}' \delta u_0 \boldsymbol{e}_y + \delta v_0 \boldsymbol{e}_x) + b_1 \mathcal{U}' u_0 \boldsymbol{e}_y + \nabla \delta p_0 \\ &- \left[(2-b_0)\nabla^2 \delta \boldsymbol{u}_b - b_1 \mathcal{U}'' \boldsymbol{e}_x - b_0 \mathcal{U} \frac{\partial \delta \boldsymbol{u}_b}{\partial x} + b_0 \mathcal{U}' \delta v_0 \boldsymbol{e}_x\right] = 0, \end{aligned} \tag{91}$$

$$\begin{aligned} &-2\nabla^2 \delta \boldsymbol{u}_b - \frac{b_0}{b_0 - 1}\left[\mathcal{U}' \delta u_0 \boldsymbol{e}_y + u_0 \nabla \delta u_b - (\mathcal{U} + u_0)\frac{\partial \delta \boldsymbol{u}_0}{\partial x}\right. \\ &\left. - u_0{}'(\delta v_b + \delta v_0)\boldsymbol{e}_x\right] - \frac{b_1}{b_0 - 1}\mathcal{U}' u_0 \boldsymbol{e}_y \\ &+ \frac{2 - b_0}{b_0 - 1}\nabla^2 \delta \boldsymbol{u}_0 + \frac{b_1(2b_0 - 3)}{(b_0 - 1)^2} u_0{}'' + \nabla \delta q \\ &- b_0 \sum_{i=1}^{2m}\left(\boldsymbol{u}_i^0 \cdot \nabla \boldsymbol{u}_i^1 + \boldsymbol{u}_i^1 \cdot \nabla \boldsymbol{u}_i^0\right) \\ &\underbrace{-b_1 \sum_{i=1}^{2m} \boldsymbol{u}_i^0 \cdot \nabla \boldsymbol{u}_i^0 - b_0 \sum_{i=2m+1}^{2m+2} \boldsymbol{u}_i^0 \cdot \nabla \boldsymbol{u}_i^0}_{\text{driving term}} = 0. \end{aligned} \tag{92}$$

Note that the part $b_1 \sum_{i=1}^{2m} \boldsymbol{u}_i^0 \cdot \boldsymbol{u}_i^0$ is one dimensional because $A_i^2 = B_i^2$ for $i = 1, 2, \ldots, m$. Like Eq. (72), the three-dimensional field is due to the driving term $\sum_{i=2m+1}^{2m+2} \boldsymbol{u}_i^0 \cdot \nabla \boldsymbol{u}_i^0$, which can be split into a one-dimensional part (proportional to $A^2_{m+1} + B^2_{m+1}$) and a two-dimensional part (proportional to $A^2_{m+1} - B^2_{m+1}$). Therefore, $\delta \boldsymbol{u}_b$ has the following general form:

$$\begin{aligned} \delta \boldsymbol{u}_b = y\boldsymbol{e}_x &+ \sum_{i=1}^{m+1}\left(A_i^2 + B_i^2\right)\boldsymbol{P}_i(y) \\ &+ \left(A^2_{m+1} - B^2_{m+1}\right)\boldsymbol{Q} + \boldsymbol{\Phi}(y, z) \end{aligned} \tag{93}$$

where $\boldsymbol{P}_i = (P_i(y), 0, 0)^T$ and $\boldsymbol{Q} = (Q_1 \cos(2k_{m+1}z), Q_2 \cos(2k_{m+1}z), Q_3 \sin(2k_{m+1}z))^T$, and $\boldsymbol{\Phi}$ collects all the other wave-number terms $(k_i \neq 2k_{m+1})$.

The spectral constraint for modes $i = 1, 2, \ldots, 2m$ at order $O(\epsilon)$ and modes $i = 2m+1$ and $2m+2$ at order $O(\epsilon^{3/2})$ is expressed as

$$\nabla \cdot \boldsymbol{u}_i^1 = 0, \tag{94}$$

$$\begin{aligned} &-2\nabla^2 \boldsymbol{u}_i^1 + b_0\left(\nabla \boldsymbol{u}_{b0} + \nabla \boldsymbol{u}_{b0}^T\right) \cdot \boldsymbol{u}_i^1 + \nabla p_i \\ &= -b_1\left(\nabla \boldsymbol{u}_{b0} + \nabla \boldsymbol{u}_{b0}^T\right) \cdot \boldsymbol{u}_i^0 - b_0\left(\nabla \delta \boldsymbol{u}_b + \nabla \delta \boldsymbol{u}_b^T\right) \cdot \boldsymbol{u}_i^0. \end{aligned} \tag{95}$$

Here $\boldsymbol{u}_{b0} = \mathcal{U}(y)\boldsymbol{e}_x$. The key issue is to examine the solvability conditions for modes $i = 2m+1$ and $2m+2$, which requires

$$\left\langle \boldsymbol{u}_i^0 \cdot \left[b_1 \mathcal{U}'\left(u_i^0 \boldsymbol{e}_z + v_i^0 \boldsymbol{e}_x\right) + b_0\left(\nabla \delta \boldsymbol{u}_b + \nabla \delta \boldsymbol{u}_b^T\right) \cdot \boldsymbol{u}_i^0\right]\right\rangle = 0. \tag{96}$$

Hence, the solvability conditions for the first order spectral constraint for the two modes yield

$$\begin{aligned} &\int_{-1}^{1} U_{m+1} V_{m+1}(b_1 \mathcal{U}' + 1) dz + \sum_{i=1}^{m+1}\left(A_i^2 + B_i^2\right) \\ &\times \int_{-1}^{1} U_{m+1} V_{m+1} P_i' dz \\ &\pm \left(A^2_{m+1} - B^2_{m+1}\right)\int_{-1}^{1} -k_{m+1} U_{m+1} W_{m+1} Q_1 + \frac{1}{2} U_{m+1} V_{m+1} Q_1{}' \\ &+ \frac{1}{2} V_{m+1} W_{m+1}(Q_3{}' - 2k_{m+1} Q_2) \\ &+ \frac{1}{2} V_{m+1}^2 Q_2{}' + k_{m+1} W_{m+1}^2 Q_3 dz = 0, \end{aligned} \tag{97}$$

where the positive or negative sign before $(A^2_{m+1} - B^2_{m+1})$ is chosen when switching $i = 2m+1$ to $i = 2m+2$. The coefficient on $(A^2_{m+1} - B^2_{m+1})$ in Eq. (97) is generically nonzero as argued previously, since one has to determine three unknowns b_1, A^2_{m+1}, and B^2_{m+1} using Eqs. (97) and (58). If the integral is zero, we will lack one condition to solve b_1, A^2_{m+1}, and B^2_{m+1}. Hence, we have to force $A^2_{m+1} = B^2_{m+1}$ such that a solution can be obtained and the background field $\boldsymbol{u}_b$ remains one dimensional at the $m+1$th bifurcation. Surprisingly, this indicates that it is impossible to lower the upper bound given by the one-dimensional background field by extending it to a three-dimensional field.

In the real observations, the flow field not only satisfies the continuity equation but also the momentum equation.

However, the present paper suggests that the upper bound theory can only impose the continuity equation and a surface averaged momentum equation as constraints. Actually, the constraints form a strict subset of those implied by the original governing equations. Therefore, the Doering-Constantin-Hopf formalism produces a higher "bound" on the momentum transfer than that realized in real observations and we are not able to observe this bound in experiments or numerical simulations because the optimal solution does not satisfy the momentum equation. However, this paper does not indicate that the ultimate scaling $\mathrm{Nu} \sim \mathrm{Ta}^{1/2}$ is not observable. Indeed, the ultimate scaling $\mathrm{Nu} \sim \mathrm{Ta}^{1/2}$ has been observed in experimental study and numerical simulations when the wall is rough [12,13]. These studies [12,13] suggested an effective approach to achieve the ultimate scaling by destroying the laminar boundary layers. Nevertheless, the scaling should still be lower than the upper bound on momentum transfer between two rough walls (this implies that the prefactor of the upper bound is larger than that found by experiments and numerical simulations).

VIII. CONCLUSION

We have investigated the upper bound on angular momentum transport in Taylor-Couette flow using a background approach. The flow is bounded between a rotating inner cylinder of radius R_i and a fixed outer cylinder of radius R_o. Both a one-dimensional background field and a three-dimensional background field were considered. For the one-dimensional background field study, a variational problem is formulated with the continuity equation and the surface-averaged momentum equation imposed as constraints. A pseudo-time-stepping method was employed to solve the resulting Euler-Lagrange equations up to Taylor number $\mathrm{Ta} = 10^9$ and three typical radius ratios $\eta = R_i/R_o = 0.5, 0.714,$ and 0.909 were examined. The results showed that the dimensionless angular momentum transport, characterized by a Nusselt number Nu, is bounded by $\mathrm{Nu} \leqslant c\mathrm{Ta}^{1/2}$. The prefactors c obtained in the present paper were found to be at least one order of magnitude lower than the rigorous upper bounds by Doering and Constantin [25] and Constantin [30].

To lower the bound, we attempted to use a three-dimensional background flow field such that the full steady momentum equation is imposed as constraint explicitly. Using an inductive bifurcation analysis, we found that, due to the solvability condition of the so-called "spectral constraint," the three-dimensional background field always regresses back to the one-dimensional situation. Therefore, imposing the full steady momentum equation as constraint is unable to lower the bound given by the one-dimensional background field. This is in agreement with the recent study of the upper bound on heat transport in Rayleigh-Bénard convection by Ding and Kerswell [35]. The present paper also indicates that there are no steady three-dimensional solutions of the Navier-Stokes equation that can produce an upper bound on the angular momentum transfer because they will not satisfy the spectral constraint.

ACKNOWLEDGMENTS

The authors acknowledge support from the Engineering and Physical Sciences Research Council Grant No. EP/P000959/1 on optimization in fluid mechanics. Z.D. also acknowledges Prof. R. R. Kerswell for initiating this study and for his many insightful comments. Finally, the authors would like to thank the referees for their many constructive suggestions.

APPENDIX A: RIGOROUS UPPER BOUND

To derive the rigorous upper bound, we follow the technique by Seis [36] instead of assuming a piecewise linear profile as Doering and Constantin [25] and Constantin [30]. Using Eq. (9), we have

$$\varepsilon = \frac{\mathrm{Re}_i J^{\omega}}{r_i\left(r_o^2 - r_i^2\right)} = \frac{\mathrm{Re}_i}{2r_i^2 + r_i}\left[r^2\left(\frac{d\overline{v}}{dr} - \frac{\overline{v}}{r}\right) - r^2\overline{uv}\right] \leqslant \frac{\mathrm{Re}_i}{2r_i^2 + r_i}\left[r^2\left(\left|\frac{d\overline{v}}{dr}\right| + \left|\frac{\overline{v}}{r}\right|\right) + r^2|\overline{uv}|\right]. \tag{A1}$$

Here, the outer cylinder is fixed.

Integration of Eq. (A1) from $r = r_o - l$ to the outer cylinder $r = r_o$ $(0 \leqslant l \leqslant 1)$ gives

$$\int_{r_o-l}^{r_o} r\varepsilon dr \leqslant \int_{r_o-l}^{r_o} \frac{\mathrm{Re}_i}{2r_i^2 + r_i}\left[r^3\left(\left|\frac{d\overline{v}}{dr}\right| + \left|\frac{\overline{v}}{r}\right|\right) + r^3|\overline{uv}|\right]dr. \tag{A2}$$

The term

$$\int_{r_o-l}^{r_o} r^3|\overline{uv}|dr \leqslant \int_{r_o-l}^{r_o} r_o^2 r|\overline{uv}|dr \leqslant \frac{1}{2\pi L}r_o^2\left(\int_{r_o-l}^{r_o} ru^2 drd\theta dz\right)^{1/2}\left(\int_{r_0-l}^{r_o} rv^2 drd\theta dz\right)^{1/2}, \tag{A3}$$

which yields

$$\int_{r_o-l}^{r_o} r^3|\overline{uv}|dr \leqslant \frac{1}{4\pi L}r_o^2\int_{r_o-l}^{r_o} r(u^2 + v^2)drd\theta dz. \tag{A4}$$

Furthermore, we use the Poincaré inequality:

$$\int rf^2 drd\theta dz \leqslant r_o\int f^2 drd\theta dz \leqslant l^2 r_o\int |\nabla f|^2 drd\theta dz \leqslant \frac{l^2 r_o}{r_i}\int r|\nabla f|^2 drd\theta dz. \tag{A5}$$

Therefore, we have

$$\int_{r_o-l}^{r_o} r^3|\overline{uv}|dr \leqslant \frac{1}{4\pi L}\frac{l^2 r_o^3}{r_i}\int_{r_o-l}^{r_o} r|\nabla \boldsymbol{u}|^2 dr d\theta dz. \tag{A6}$$

The term

$$\int_{r_o-l}^{r_o}\left[r^3\left|\frac{d\overline{v}}{dr}\right|\right]dr \leqslant \frac{1}{2\pi L}l^{1/2}r_o^{5/2}\left(\int r\left|\frac{dv}{dr}\right|^2 dr d\theta dz\right)^{1/2} \leqslant \frac{1}{2\pi L}l^{1/2}r_o^{5/2}\left(\int r|\nabla \boldsymbol{u}|^2 dr d\theta dz\right)^{1/2}. \tag{A7}$$

The term

$$\int_{r_o-l}^{r_o} r^2|\overline{v}|dr \leqslant \frac{1}{2\pi L}l^{1/2}r_o^{3/2}\left(\int rv^2 dr d\theta dz\right)^{1/2} \leqslant \frac{1}{2\pi L}l^{3/2}\frac{r_o^2}{r_i^{1/2}}\left(\int r|\nabla \boldsymbol{u}|^2 dr d\theta dz\right)^{1/2}. \tag{A8}$$

Therefore, we have

$$2r_i l\varepsilon \leqslant \frac{\mathrm{Re}_i}{4\pi L}\frac{l^2 r_o^3}{r_i^3}\mathbb{P} + \frac{\mathrm{Re}_i}{2\pi L}\left(\frac{l^{1/2}r_o^{5/2}}{r_i^2} + \frac{l^{3/2}r_o^2}{r_i^{5/2}}\right)\mathbb{P}^{1/2} \tag{A9}$$

where $\mathbb{P}^{1/2} = \int_{r_o-l}^{r_o} r|\nabla \boldsymbol{u}|^2 dr d\theta dz$.

Noting that

$$\varepsilon = \langle|\nabla \boldsymbol{u}|^2\rangle + 2\frac{\mathrm{Re}_i^2}{r_o^2 - r_i^2}, \tag{A10}$$

we have

$$\varepsilon \leqslant \frac{\mathrm{Re}_i}{4}\frac{l r_o^3}{r_i^4}\varepsilon + \frac{\mathrm{Re}_i}{l^{1/2}}\frac{r_o^{5/2}}{r_i^3}\varepsilon^{1/2}. \tag{A11}$$

We choose the value of l such that the right-hand side is minimal, then $l \sim \varepsilon^{-1/3}$. Hence, we have $\varepsilon \leqslant \text{const} \times \mathrm{Re}_i^3$, which yields $\mathrm{Nu} \leqslant \text{const} \times \mathrm{Ta}^{1/2}$.

APPENDIX B: THE EIGENVALUES

Here, we show the numerical evidence that the most unstable mode of the spectral constraint is always x independent (see Fig. 9). To check the spectral constraint Eqs. (23) and (24), we introduce the disturbance in the form of

$$\hat{\boldsymbol{u}} = \hat{\boldsymbol{u}}_{mn}\exp(im\theta + ik_n z). \tag{B1}$$

When a background flow field is obtained numerically, we can check if the spectral constraint is satisfied for all m and k_n.

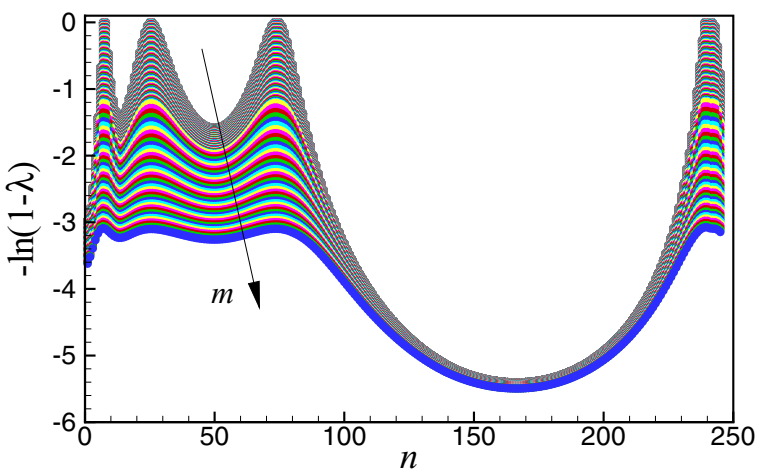

FIG. 9. The shifted eigenvalue vs the wave number n of the Taylor-Couette flow at $\eta = 0.99$ and $\mathrm{Re} = 10^4$. The aspect ratio $\Gamma = 10$ and the azimuthal wave number is increased from $m = 0$ to 300.

[1] F. Wendt, Turbulente Strömungen zwischen zwei rotierenden Zylindern, Ingenieurs-Archiv **4**, 577 (1933).

[2] C. Andereck, S. Liu, and H. Swinney, Flow regimes in a circular Couette system with independently rotating cylinders, J. Fluid Mech. **164**, 155 (1986).

[3] M. Burin, E. Schartman, and H. Ji, Local measurements of turbulent angular momentum transport in circular Couette flow, Exp. Fluids **48**, 763 (2010).

[4] D. van Gils, S. Huisman, G. Bruggert, C. Sun, and D. Lohse, Torque Scaling in Turbulent Taylor-Couette Flow with Co- and Counter-Rotating Cylinders, Phys. Rev. Lett. **106**, 024502 (2011).

[5] M. Paoletti and D. Lathrop, Angular Momentum Transport in Turbulent Flow Between Independently Rotating Cylinders, Phys. Rev. Lett. **106**, 024501 (2011).

[6] S. Huisamn, D. van Gils, S. Grossmann, C. Sun, and D. Lohse, Ultimate Turbulent Taylor-Couette Flow, Phys. Rev. Lett. **108**, 024501 (2012).

[7] R. Ezeta, S. Huisman, C. Sun, and D. Lohse, Turbulence strength in ultimate Taylor-Couette turbulence, J. Fluid Mech. **836**, 397 (2018).

[8] B. Eckhardt, S. Grossmann, and D. Lohse, Torque scaling in turbulent Taylor-Couette flow between independently rotating cylinders, J. Fluid Mech. **581**, 221 (2007).

[9] S. Grossmann, D. Lohse, and C. Sun, High-Reynolds number taylor-couette turbulence, Annu. Rev. Fluid Mech. **48**, 53 (2016).

[10] O. Cadot, Y. Couder, A. Daerr, S. Douady, and A. Tsinober, Energy injection in closed turbulent flows: Stirring through boundary layers versus inertial stirring, Phys. Rev. E **56**, 427 (1997).

[11] G. S. Lewis and H. L. Swinney, Velocity structure functions, scaling, and transitions in high-Reynolds-number Couette-Taylor flow, Phys. Rev. E **59**, 5457 (1999).

[12] T. van den Berg, C. D. D. Lohse, and D. Lathrop, Smooth and rough boundaries in turbulent Taylor-Couette flow, Phys. Rev. E **68**, 036307 (2003).

[13] X. Zhu, R. A. Verschoof, D. Bakhuis, S. G. Huisman, R. Verzicco, C. Sun, and D. Lohse, Wall roughness induces asymptotic ultimate turbulence, Nat. Phys. **14**, 417 (2018).

[14] H. Brauckmann and B. Eckhardt, Direct numerical simulations of local and global torque in Taylor-Couette flow up to Re = 30 000, J. Fluid Mech. **718**, 398 (2013).

[15] S. Merbold, H. Brauckmann, and C. Egbers, Torque measurements and numerical determination in differentially rotating wide gap Taylor-Couette flow, Phys. Rev. E **87**, 023014 (2013).

[16] R. Ostilla-Mónico, S. Grossmann, R. Verzicco, and D. Lohse, Optimal Taylor-Couette flow: Direct numerical simulations, J. Fluid Mech. **719**, 14 (2013).

[17] R. Ostilla-Mónico, R. Huisman, S. Jannink, T. van Gils, S. Grossmann, R. Verzicco, C. Sun, and D. Lohse, Optimal Taylor-Couette flow: Radius ratio dependence, J. Fluid Mech. **747**, 1 (2014).

[18] R. Ostilla-Mónico, E. van der Poel, R. Verzicco, S. Grossmann, and D. Lohse, Boundary layer dynamics at the transition between the classical and the ultimate regime of Taylor-Couette flow, Phys. Fluids **26**, 015114 (2014).

[19] R. Ostilla-Mónico, E. van der Poel, R. Verzicco, S. Grossmann, and D. Lohse, Exploring the phase diagram of fully turbulent Taylor-Couette flow, J. Fluid Mech. **761**, 1 (2014).

[20] W. Malkus, The heat transport and spectrum of thermal turbulence, Proc. R. Soc. A **225**, 196 (1954).

[21] L. Howard, Heat transport by turbulent convection, J. Fluid Mech. **17**, 405 (1963).

[22] F. Busse, On Howard's upper bound for heat transport by turbulent convection, J. Fluid Mech. **37**, 457 (1969).

[23] E. Nickerson, Upper bounds on the torque in cylindrical Couette flow, J. Fluid Mech. **38**, 807 (1969).

[24] F. Busse, The bounding theory of turbulence and its physical significance in the case of turbulent Couette flow, Statistical Models and Turbulence **12**, 103 (1972).

[25] C. Doering and P. Constantin, Energy Dissipation in Shear Driven Turbulence, Phys. Rev. Lett. **69**, 1648 (1992).

[26] C. Doering and P. Constantin, Variational bounds on energy dissipation in incompressible flows: Shear flow, Phys. Rev. E **49**, 4087 (1994).

[27] C. Doering and P. Constantin, Variational bounds on energy dissipation in incompressible flows. III. Convection, Phys. Rev. E **53**, 5957 (1996).

[28] R. Kerswell, Variational bounds on shear-driven turbulence and turbulent Boussinesq convection, Physica D **100**, 355 (1997).

[29] R. Kerswell, Unification of variational principles for turbulent shear flows: The background method of Doering-Constantin and Howard-Busse's mean-fluctuation formulation, Physica D **121**, 175 (1998).

[30] P. Constantin, Geometric statistics in turbulence, SIAM Rev. **36**, 73 (1994).

[31] S. Plasting and R. Kerswell, Improved upper bound on the energy dissipation rate in plane Couette flow: The full solution to Busse's problem and the Constantin-Doering-Hopf problem with one-dimensional background field, J. Fluid Mech. **477**, 363 (2003).

[32] B. Wen, G. Chini, N. Dianati, and C. Doering, Computational approaches to aspect-ratio-dependent upper bounds and heat flux in porous medium convection, Phys. Lett. A **377**, 2931 (2013).

[33] B. Wen, G. Chini, R. Kerswell, and C. Doering, Time-stepping approach for solving upper-bound problems: Application to two-dimensional Rayleigh-Bénard convection, Phys. Rev. E **92**, 043012 (2015).

[34] G. Fantuzzi, Construction of optimal background fields using semidefinite programming, Ph.D. thesis, Imperial College, 2018.

[35] Z. Ding and R. Kerswell, Exhausting the background approach for bounding the heat transport in Rayleigh-Bénard convection, J. Fluid Mech. (to be published) (2020).

[36] C. Seis, Scaling bounds on dissipation in turbulent flows, J. Fluid Mech. **777**, 591 (2015).